Powerful and accurate detection of temporal gene expression patterns from multi-sample multi-stage single-cell transcriptomics data

Yue Fan[1,2], Lei Li[1,2], and Shiquan Sun[1,2,3,*]

1. Center for Single-Cell Omics and Health, School of Public Health, Xi'an Jiaotong University, Xi'an, Shaanxi 710061, P.R. China

2. Collaborative Innovation Center of Endemic Diseases and Health Promotion in Silk Road Region and Key Laboratory of Trace Elements and Endemic Diseases, Xi'an Jiaotong University, Xi'an, Shaanxi 710061, P.R. China

3. Key Laboratory for Disease Prevention and Control and Health Promotion of Shaanxi Province, Xi'an, Shaanxi 710061, P.R. China

* Correspondence to: SS (Email: sqsunsph@xjtu.edu.cn)

ABSTRACT

The advanced single-cell RNA sequencing (scRNA-seq) technology allows us to measure the temporal dynamics of gene expression over multiple time points to gain an understanding of previously unknown biological diversity. However, there is currently a lack of efficient computational tools tailored for scRNA-seq data analysis, which can simultaneously analyze the entire sequence across different time points as well as accounting for temporal batch effects.

In this paper, we present a non-parametric statistical method called TDEseq that takes full advantage of smoothing splines basis functions to account for the dependence of multiple time points, and uses hierarchical structure linear additive mixed models to model the correlated cells within an individual. As a result, TDEseq demonstrates powerful performance in identifying four potential temporal expression patterns within a specific cell type, including growth, recession, peak, and trough. Extensive simulation studies and the analysis of four published scRNA-seq datasets show that TDEseq can produce well-calibrated *p*-values and up to 20% power gain over the existing methods for detecting temporal gene expression patterns, even with the case in large heterogeneous.

TDEseq is also capable of handling unwanted confounding factors that may be hidden in biological processes, thereby enabling advancements in investigations that utilize time-resolved or time-course scRNA-seq data, particularly in the multi-sample multi-stage studies.

KEYWORDS: time-resolved scRNA-seq data; time-course scRNA-seq data; temporal expression patterns; non-parametric models.

INTRODUCTION

The advances in single-cell RNA sequencing (scRNA-seq) technologies make it possible to record the temporal dynamics of gene expression over multiple time points or stages either in the same cell population [1, 2] or even in an individual cell without destruction [3]. Unlike the single time point (e.g., snapshot) profiling of transcriptome that allocates cells on pseudotime or lineages using purely computational strategies [4-6], in particular, the time-resolved or time-course scRNA-seq profiling of whole transcriptome with respect to real, physical time, is capable of providing additional insights into dynamic biological processes [2, 7]. For example, how the cells naturally differentiate into other types or states during the development processes and how the cellular response to specific drug treatments [8], viral infections [9], etc. Therefore, accurately characterizing the temporal dynamics of gene expression over time points is crucial for developmental biology [10, 11], tumor biology [12-14], and biogerontology [15-17], which allows us to decipher the dynamic cellular heterogeneity during cell differentiation [18]; identifying cancer driver genes during the status transformation [14]; and investigating the mechanisms of cell senescence during aging [15]. Although the time-resolved and time-course scRNA-seq studies are initially designed for different purposes, they both require the same data analysis tools for detecting the temporal dynamics of gene expression [19]. As we know, the statistical modeling for both types of scRNA-seq data to identify temporal gene expression patterns meets significant challenges, i.e., modeling unwanted variables, accounting for temporal dependencies, and even characterizing non-stationary cell populations of scRNA-seq data. However, existing methods are unable to fully consider these limitations, resulting it remains an urgent need to develop effective tools for detecting temporal dynamics of gene expression in both time-resolved and time-course scRNA-seq studies.

Particularly, both time-resolved and time-course scRNA-seq data commonly share a fundamental temporal nature, i.e., the gene expression levels measured at each time point may be influenced by previous time points. Accounting for these temporal dependencies requires specialized statistical and computational tools [20], and failure to do so can lead to inaccurate gene detections [21, 22]. As a result, current temporal gene detection methods for time-resolved or time-course scRNA-seq data can be divided into two categories: the methods that treat time points independently and methods that model the temporal dependencies explicitly. Specifically, the methods that utilize the former approach are mostly treated time

as a categorical variable, performing the differential expression analysis with pair-wise comparison using a two-sided *Wilcoxon* rank-sum test [23, 24], DESeq2 [25, 26], or edgeR [27, 28], etc. However, neglecting the temporal dependencies among multiple time points will reduce the statistical power and may lead to false-positive results [22]. On the other hand, the methods that utilize the latter approach are commonly used for addressing the time-course bulk RNA-seq data, such as ImpulseDE2 [29], and maSigPro [30, 31]. However, the scRNA-seq data is often sparse along with technical and biological variability, making it difficult to accurately identify true biological gene expression changes over multiple time points [32, 33].

Furthermore, both time-resolved and time-course scRNA-seq data are often collected from multi-sample multi-stage designs. As a result, there may be unwanted variables that arise due to technical variability, batch effects, or the genetic background of individuals [34]. These variables can obscure the temporal changes in gene expression that are of interest, making it challenging to detect temporal expression change accurately. Alternatively, the trajectory-based differential expression analysis methods, such as Monocle2 [5], tradeSeq [35], and PseudotimeDE [36] could detect the temporal dynamics of gene expressions along with pseudotime or a continuous trajectory of cellular states. However, since the gene expression profiles of cells from the same sample/individual are known to be dependent, these methods may not adequately account for technical or biological variability that may present in multi-sample multi-stage designs. In addition, these methods may not fully capture the underlying biological process at specific tipping points or intervals, which could be particularly relevant in understanding the mechanisms of cell fate or differentiation [37, 38], and tumor progression [14].

Here, to properly address the above challenges, we develop an efficient and flexible non-parametric method for detecting the temporal expression patterns over multiple time points (also denoted as temporal dynamics of expression analysis). We refer to our method as *TDEseq*, Temporal Differentially Expressed genes of time-resolved and time-course scRNA-seq data. Specifically, TDEseq primarily builds upon the linear additive mixed model (LAMM) framework, with a random effect term to account for correlated samples in time-resolved or time-course scRNA-seq studies. In this model, we typically introduce the quadratic *I*-splines [39] and cubic *C*-splines [40] as basis functions, which facilitate the detection of four potential temporal gene expression patterns, i.e., growth, recession, peak, and trough. As a result, with extensive simulation studies, we find TDEseq can properly control for type I error rate at the transcriptome-wide level, and display powerful

performance in detecting temporal expression genes under the power simulations. Finally, we apply the TDEseq to one time-resolved scRNA-seq data set which was generated by Well-TEMP-seq [23] from human colorectal cancer HCT116 cells, and three time-course scRNA-seq data sets to benchmark TDEseq against current state-of-the-art methods, regarding mouse hepatocyte differentiation [41], human metastatic lung adenocarcinoma [14] and human COVID-19 progression [9]. These results highlight TDEseq is an appropriate tool for detecting temporal dynamics of gene expression over multiple time points, which leads to an improved understanding of developmental biology, tumor biology, and biogerontology.

RESULTS

Overview of TDEseq

Statistical modeling: TDEseq is a temporal gene expression analysis approach that is primarily built upon the linear additive mixed models (LAMM) [42] framework to characterize the temporal gene expression changes for time-resolved and time-course (or longitudinal) scRNA-seq data sets (Materials and Methods; Supplementary Text). Typically, we aim to detect one of four possible temporal gene expression patterns (i.e., growth, recession, peak, or trough) over multiple time points using both *I*-splines [39] and *C*-splines [40] basis functions (Figure 1A), and examine one gene at a time. Briefly, In LAMM, we assume the transformed gene expression of raw count data (Materials and Methods), i.e., y_{gji} for gene g, individual j and cell i at time t is,

$$y_{gji} = \boldsymbol{w}_{gji}\boldsymbol{\alpha}_g + \sum_{k=1}^{K} s_k(t)\beta_{gk} + u_{gj} + e_{gji},\ i = 1,2,\cdots,N; g = 1,2,\cdots,G; t = 1,2,\cdots,T, j = 1,\dots,M$$

where $\boldsymbol{w}_{gji}$ is the cell-level or time-level covariate (e.g., cell size, or sequencing read depth), $\boldsymbol{\alpha}_g$ is its corresponding coefficient; $\boldsymbol{u}_g$ is a random vector to account for the variations from heterogeneous samples, i.e.,

$$\boldsymbol{u}_{gj} \sim MVN\left(0, \sigma_{gu}^2 \boldsymbol{\Sigma}_{n_j \times n_j}\right), j = 1,\dots,M$$

where n_j is the number of cells for the individual or replicate j and $\sum_{j=1}^{M} n_j = N$, $\boldsymbol{\Sigma}_{n_j \times n_j}$ is a $n_j \times n_j$ all-ones matrix; e_{gi} is a random effect, which is an independent and identically distributed variable that follows a normal distribution with mean zero and variance σ_g^2 to account for independent noise, i.e.,

$$\boldsymbol{e}_g = \left(e_{g1},\cdots,e_{gN}\right)' \sim MVN(0, \sigma_g^2 \mathbf{I}_{r\times r})$$

Particularly, the variable $s_k(t)$ is a smoothing spline basis function, which involves either *I*-splines or *C*-splines to model monotone patterns (i.e., growth and recession) and concave/convex patterns (i.e., peak and trough), respectively [43] (Figure 1A). The *I*-splines are defined as $I_l^k(x) = \int_{\xi_1}^{x} M_{t1}^k(v)dv$ [39]; while *C*-splines are defined as $C_l^k(x) = \int_{\xi_1}^{x} I_{t1}^k(v)d(v)$ [40] based on *I*-splines, and β_{gk} is its corresponding coefficient that is restricted to $\beta_{gk} \geq 0$, and $l\ (l = 1,2,\cdots,L)$ is the number of grid points. We set L to be a total number of grid points in scRNA-seq data, which is equal to the number of time points in practice; k denotes the order of the spline function; MVN denotes the multivariate normal distribution.

Hypothesis testing: in the LAMM model mentioned above, we are interested in examining whether a gene shows one of four temporal expression patterns, i.e.,

growth, recession, peak, or trough (Figure 1A). Testing whether a gene expression displays temporal dynamics of gene expression can be translated into testing the null hypothesis $\mathbf{H_0}: \boldsymbol{\beta}_g = 0$. Parameter estimates and hypothesis testing in LAMM are notoriously difficult, as the LAMM likelihood involves *M*-splines [39] (non-linear) subject to nonnegative constraints that cannot be solved analytically. To make the LAMM model scalable estimation and inference, we developed an approximate inference algorithm based on the cone programming projection algorithm [44]. With parameter estimates, we computed a *p*-value for each of the four patterns using the test statistics [45], which follow a mixture of beta distributions [46]. Afterward, we combined these four *p*-values through the Cauchy combination rule [47]. The Cauchy combination rule allows us to combine multiple potentially correlated *p*-values into a single *p*-value to determine whether a gene is a temporal expression gene or not (Materials and Methods; Supplementary Text).

We refer to the above method as the mixed version of TDEseq (we denoted as *Mixed TDEseq*). Besides the mixed version, we have also developed a linear version of TDEseq (to distinct Mixed TDEseq, which we denoted as *Linear TDEseq*) for modeling the small or no batch effects inherited in time-resolved or time-course scRNA-seq data sets (Supplementary Text). Both versions of TDEseq were implemented in the same R package with multiple threads computing capability. The software TDEseq, together with all reproducibility analysis code are freely available at https://sqsun.github.io/software.html.

TDEseq generates well-calibrated *p*-values and exhibits powerful gene detection of temporal expression changes in simulations

To benchmark the robustness and performance of TDEseq, we simulated extensive scRNA-seq data sets using the *Splatter* R package [48], and compared two versions of TDEseq with three existing approaches but not specific designs for time-resolved or time-course scRNA-seq data analysis, which are a two-sided Wilcoxon rank-sum test (Wilcoxon test), tradeSeq [49], and ImpulseDE2 [29] (Materials and Methods). The simulations were typically designed to assess the ability of TDEseq in terms of type I error control rate and temporal gene detection power with varying various parameter settings, including the number of time points (i.e., 4, 5, or 6), the number of cells for each individual (i.e., 50, 100, or 200, individual in each time point), the expected UMI counts for each cell of scRNA-seq data (i.e., 7.0 as low, 9.7 as medium, and 13.8 as high), the effect size of temporal expression changes (i.e., 0.1 as low, 0.4 as medium, and 0.7 as high), and the batch effect size across time points (i.e., 0% of effect size as no batch effects, 10%

of effect size as medium and 30% of effect size as high).

To do so, we considered a baseline simulation scenario: the number of time points as 5, the number of cells in each time point as 300, the expected UMI counts for each cell as 9.7, the effect size of temporal expression changes as 0.4; the batch effect size as 0.04; all cells were measured by 10,000 genes, in which 1,000 genes were randomly assigned one of four possible temporal patterns (i.e., growth, recession, peak, and trough) in power simulations. With the baseline parameter settings, we varied one parameter at a time to examine whether the gene is temporally expressed over multiple time points. Notably, here all baseline parameters were estimated from the lung adenocarcinoma progression scRNA-seq data [14] (Materials and Methods).

With the baseline parameter setup, we found that only Mixed TDEseq generated the well-calibrated *p*-values under the null simulations, whereas all other methods produced the inflated *p*-values (Figure 1B). Besides, for the power simulations, Linear TDEseq and Mixed TDEseq can produce a more powerful temporal expression pattern detection rate across a range of FDR cutoffs (Figure 1C). Specifically, with a false discovery rate (FDR) of 5%, the power detection rate of both Linear and Mixed TDEseq were 43.3% and 40.8%, respectively, followed by tradeSeq was 25.9% and ImpulseDE2 was 18.4%. Furthermore, we also examined the accuracy of pattern detection, finding both linear and mixed versions of TDEseq outperformed ImpluseDE2 (could detect pattern-specific genes). Specifically, with an FDR of 5%, the averaged accuracy of detection power (with 10-time repeats) for Mixed TDEseq achieved 99.0% for growth, 100% for recession, 80.4% for peak, and 43.6% for trough. In contrast, ImpulseDE2 achieved 73.1% for growth, 83.5% for recession, 39.3% for peak, and 21.3% for trough (Figure 1D).

In addition, we systematically examined the performance of the type I error control rate under other parameter settings. Our findings indicate that Mixed TDEseq consistently produces well-calibrated *p*-values (Figures S1A, S1B, S2A, S3A, and S3B) except when dealing with high UMI counts (Figure S2B). These observations are presumably due to the presence of unwanted batch effects associated with high UMI counts. On the other hand, in terms of temporal expression gene detection and averaged accuracy of pattern detection, both Mixed TDEseq and Linear TDEseq display powerful performance across a range of parameter settings regardless of the number of time points (Figure S1), the expected UMI counts for

each cell (Figure S2), the number of cells in each time point (Figure S3) and the effect size setups (Figure S4), as well as accurately pattern detection (Figure S5). Notably, the Wilcoxon test did not fare well in all power simulations, presumably due to failure to properly control the type I error rate.

TDEseq coupled with batch removal strategy exhibits excellent performance in analyzing large heterogeneous scRNA-seq data

Intuitively, in situations with minimal or no batch effects, it is reasonable to expect that trajectory-based differential expression methods (e.g., tradeSeq) would yield comparable results to temporal-based differential expression methods. To do so, we reduced the batch effect size to be zero. As a result, we observed that both versions of TDEseq and tradeSeq generated well-calibrated *p*-values under the null simulations, whereas ImpulseDE2 demonstrated the overly conservative *p*-values and the Wilcoxon test displays the inflated *p*-values (Figure S6A). Again, both versions of TDEseq and all other approaches gained a comparable detection rate power (Figure S6B). As we know, the presence of unwanted batch effects poses substantial obstacles in detecting temporal expression changes. We therefore increased the batch effect size to 30%, and found Mixed TDEseq could outperform other methods in terms of temporal expression pattern detection power (Figure 1F). However, the *p*-values generated by Mixed TDEseq were not well-calibrated (Figure 1E).

To this end, to properly control the unwanted variables in the large batch effects scenario, we additionally carried out the batch correction procedure prior to performing temporal gene expression detection. To do so, we benchmarked five existing batch removal methods which can return the corrected gene expression matrix, including MNN [50], scMerge [51], ZINB-WaVE [52], ComBat [53], and Limma [54]. As a result, with evaluation criterion iLISI score [55] (Materials and Methods) for batch correction approaches, we found scMerge (0.49) achieved a higher alignment score than Limma (0.48), ComBat (0.48), MNN (0.11), and ZINB-WaVE (0.21; Figure S7). Moreover, we found Mixed TDEseq coupled with scMerge (Mixed TDEseq + scMerge; purple line) performed reasonably well in terms of the type I error control (Figures 1E and S8A) and more powerful in detecting temporal expression genes (Figures 1F and S8B), suggesting this combination is suitable for time-course scRNA-seq data with strong batch effects. Taken together, TDEseq coupled with scMerge may be an ideal approach for the identification of temporal gene expression patterns when time-course scRNA-seq data involves large heterogeneous samples.

TDEseq detects drug-associated temporal expression changes of time-resolved scRNA-seq data

We first applied TDEseq on a drug-treatment time-resolved scRNA-seq data set. The data were assayed by Well-TEMP-seq protocols to profile the transcriptional dynamics of colorectal cancer cells exposed to 5-AZA-CdR [23] (Materials and Methods; Table S1). This scRNA-seq data set consists of D0, D1, D2, and D3 four time points (Figures 2A and S9A), and each time point contains 4,000 cells. We expected these scRNA-seq data sets to exhibit minimal batch effects across multiple time points since Well-TEMP-seq addressed the cell lines within one chip [23]. Therefore, we performed the temporal gene detection methods without batch effects correction. Since only one sample was involved in each time point, we only performed Linear TDEseq in this application.

Next, we examined the ability of Linear TDEseq in terms of type I error control. To do so, we utilized a permutation strategy (repeat 5 times) to construct null distribution (Materials and Methods). Consistent with simulation studies, we found Linear TDEseq can produce well-calibrated *p*-values while tradeSeq produced inflated *p*-values and ImpulseDE2 produced overly conserved *p*-values (Figure 2B). Besides, in terms of temporally expressed gene detection, Linear TDEseq outperformed other methods across a range of FDR cutoffs (Figures 2C and S9B). For example, Linear TDEseq identified a total of 5,596 temporally expressed genes at an FDR of 5%, including 1,341 growth genes, 1,177 recession genes, 225 trough genes, and 2,853 peak genes, which displayed four distinct temporal patterns (Figure 2D). In contrast, ImpulseDE2 identified a total of 4,792 temporally expressed genes and tradeSeq detected a total of 2,672 temporally expressed genes (Table S2). Overall, besides the 2,427 common shared temporally expressed genes detected by 3 methods (Figure 2E), a total of 559 temporally expressed genes were uniquely detected by TDEseq, which were also significantly enriched in cell cycle DNA replication (GO:0044786; BH adjusted *p*-value = 7.89e-e) and response to interleukin1(GO:0070555; BH adjusted *p*-value = 0.031). In contrast, tradeSeq or ImpulseDE2 unique genes were not enriched in 5-AZA-CdR treatment response associated GO terms (Figure 2E). Specifically, we found tumor suppressor genes which were a target of 5-AZA-CdR, i.e., *DKK1* [23, 56] was identified by TDEseq as top-ranked significant temporal expression genes (*p*-value < 1e-300, FDR = 0), while was not detected by tradeSeq (*p*-value = 0.82, FDR = 0.90; Figure 2F), probably due to though this gene had clearly peak pattern, the log fold change was small enough, and difficult to detect with penalized splines;

Besides, a 5-AZA-CdR response gene *IFITM3* [56, 57] was also identified by TDEseq as top-ranked significant genes (*p*-value < 1e-300, FDR = 0), but not detected by tradeSeq (*p*-value = 0.19, FDR = 0.36, Figure 2F).

Finally, we performed gene set enrichment analysis (GSEA) on the pattern-specific temporal expression genes to examine top GO terms enriched by the given gene lists (Materials and Methods). Specifically, with an FDR of 5%, a total of 1,341 growth-specific temporal expression genes were detected by Linear TDEseq. These genes were enriched in a total of 179 GO terms. Due to 5-AZA-CdR treatment leads HCT116 cells to a viral mimicry state, and triggers the antiviral response [58], we expected as a result of an immune response that drives the immune-associated genes up-regulated. Indeed, the GO terms contain many immune response terms, such as the cell activation involved in the immune response process (GO: 0002263; BH-adjusted *p*-value = 8.90e-7), indicating immune response was activated by the 5-AZA-CdR treatment; a total of 1,177 recession-specific temporal expression genes were enriched in a total of 244 GO terms, e.g., many regulations of histone methylation terms such as positive regulation of histone H3-K4 methylation (GO: 0051571; BH-adjusted *p*-value = 0.047), implying DNA methylation inhibitions and gene expression regulation were occurred after 5-AZA-CdR treatment, due to the global DNA demethylation effects of 5-AZA-CdR [59]; a total of 2,853 peak-specific temporal expression genes were enriched in a total of 249 GO terms. For example, The ATP metabolic process pathways, particularly oxidative phosphorylation (GO: 0006119; BH-adjusted p-value = 3.30e-7), are impacted by the increase of intracellular ROS and mitochondrial superoxide induced by 5-AZA-CdR. However, this effect diminishes over time [60]; Similarly, a total of 225 trough-specific temporal expression genes were enriched in a total of 89 GO terms, with a significant portion belonging to cell cycle pathways, including mitotic nuclear division (GO: 0140014; BH-adjusted p-value = 1.06e-6). These findings suggest that 5-AZA-CdR treatment may lead to the suppression of tumor cell proliferation and division [58] (Figure 2G).

TDEseq detects hepatic cell differentiation-associated temporal expression genes of time-course scRNA-seq data

We next applied TDEseq to a hepatoblast-to-hepatocyte transition study from the C57BL/6 and C3H embryo mice livers [41] (Materials and Methods; Table S1). This scRNA-seq data set consists of 7 developmental stages from 13 samples, including E10.5 (54 cells from 1 sample), E11.5 (70 cells from 2 samples), E12.5 (41 cells from 2 samples), E13.5 (65 cells from 2 samples), E14.5 (70 cells from 2

samples), E15.5 (77 cells from 2 samples), and E17.5 (70 cells from 2 samples) [61] (Figure 3A). Compared with the above time-resolved scRNA-seq data, this time-course scRNA-seq data set contains multiple samples at each time point, exhibiting small batch effects across all developmental stages (Figure S10A). Therefore, we carried out both versions of TDEseq that would be expected to be comparable in such a scenario.

To do so, we first examined the ability of TDEseq in terms of type I error control using permutation strategies (Materials and Methods). Consistent with the simulation results, Linear TDEseq, Mixed TDEseq, and tradeSeq could produce the well-calibrated *p*-values whereas ImpulseDE2 generated overly conservative *p*-values (Figure 3B). Besides, in terms of temporally expressed gene detection, both versions of TDEseq outperformed other methods across a range of FDR cutoffs (Figures 3C and S10B). Specifically, Linear TDEseq identified a total of 9,975 temporally expressed genes at an FDR of 5%, including 1,266 growth genes, 7,146 recession genes, 217 trough genes, and 1,346 peak genes, which were displayed four temporal distinct patterns (Figure 3D); Mixed TDEseq identified a total of 8,924 temporally expressed genes, including 1,242 growth genes, 6,708 recession genes, 136 trough genes and 8,38 peak genes. In contrast, ImpulseDE2 detected a total of 7,737 temporally expressed genes while tradeSeq detected a total of 7,108 temporally expressed genes (Table S3). Notably, comparing with tradeSeq and ImpulseDE2, there were a total of 948 temporally expressed genes uniquely detected by Linear TDEseq at an FDR of 5% and a total of 3,517 temporally expressed genes uniquely detected by Mixed TDEseq at an FDR of 5% (Figure 3E and S10E). Comparing the results of Linear TDEseq and Mixed TDEseq, we found the *p*-values generated from both Mixed TDEseq and Linear TDEseq demonstrated a high correlation (Spearman R = 0.954; Figure S10C). Moreover, the temporally expressed genes detected by both versions of TDEseq but not detected by tradeSeq or ImpulseDE2 were highly related to hepatic cell differentiation (Figure 3E and S10E), many of which have been validated by existing work [41, 62, 63]. For example, we found a key mouse fetal liver development regulator *Atf4* [63], which exhibits growth pattern (Figure 3F), was only identified by TDEseq as the top-ranked significant temporal expression gene (*p*-value < 1e-300, FDR = 0), while was not detected by tradeSeq (*p*-value = 0.240, FDR = 0.275) and ImpulseDE2 (*p*-value = 0.243, FDR = 0.079). Besides, *Itgb1* displays the growth pattern (Figure 3F) for liver microstructure establishment during the embryonic process, which was only identified by TDEseq as the top-

ranked significant temporal expression gene (*p*-value < 1e-300, FDR = 0), while was not detected by tradeSeq (*p*-value = 0.272, FDR = 0.309). These genes uniquely detected by Linear TDEseq were enriched in the liver embryo process, particularly cell cycle process (GO:0022402, BH-adjusted *p*-value=1.33e-5) and embryo development (GO:0009790; BH-adjusted *p*-value = 0.0361); whereas the temporal expression genes uniquely detected by tradeSeq or ImpulseDE2 were not enriched in liver development-related functional gene sets (Figure 3E). Similar result was also observed for Mixed TDEseq unique genes (Figure S10E).

Finally, we performed GSEA on the pattern-specific temporal expression genes identified by Linear TDEseq, to examine the four pattern-specific functions during hepatic cell differentiation (Materials and Methods). Specifically, with an FDR of 5%, a total of 1266 growth-specific temporal expression genes were enriched in a total of 685 GO terms. Notably, these growth-related genes were significantly enriched in liver function-associated pathways, reflecting the mature process from hepatoblasts to hepatocytes. For example, almost all of these enriched terms were associated with metabolic processes, biosynthetic processes, or organic substance transport, with key functions attributed to mature hepatocytes (Figure 3G). Particularly, the fatty acid metabolic process (GO:0006631; BH-adjusted *p*-value = 4.99e-37), lipid catabolic process (GO:0016042; BH-adjusted *p*-value = 3.34e-26), and secondary alcohol metabolic process (GO:1902652; BH-adjusted *p*-value = 8.06e-16), which are the main function of mature hepatocytes. On the other hand, a total of 7,146 recession-specific temporal expression genes were enriched in 1,000 GO terms. Interestingly, these GO terms were related to embryo or tissue development (Figure 3G), such as embryonic morphogenesis (GO:0048598; BH-adjusted *p*-value = 1.04e-3) and mesoderm morphogenesis (GO:0048332; BH-adjusted *p*-value = 4.05e-3). This finding suggests the involvement of an embryo development process, possibly linked to organogenesis occurring at the E14.5 stage [64]. Furthermore, these genes may signify the loss of embryonic cell identity in mature hepatocytes. By contrast, although ImpulseDE2 detected more growth genes than Linear TDEseq and Mixed TDEseq (Figure S10B), we found that ImpulseDE2 wrongly detected the peak or trough genes as growth genes (Figure S10D). This phenomenon was consistent with simulation results (Figure S5).

Taken together, we found both versions of TDEseq yields similar results in terms of type I control rate and temporal expression gene detection when scRNA-seq data exhibits small batch effects over time points. Therefore, considering the

computation burden for large-scale scRNA-seq data applications, we recommended Linear TDEseq in a small batch effects scenario.

TDEseq detects the epithelial cell evaluation-associated temporal expression genes of time-course scRNA-seq data

We again applied TDEseq to detect temporal expression genes altered in human metastatic lung adenocarcinoma (LUAD) cancer [14]. Here, we were primarily interested in epithelial cells of this time-course scRNA-seq data, which involves a total of five distinct evolution stages, i.e., stage normal, stage I, stage II and stage III and stage IV (Materials and Methods; Table S1). Since stage II contains a relatively small number of cells (i.e., 119 cells), we excluded this stage, resulting in a total of 3,703 cells from 11 samples in the normal stage, 5,651 cells from 8 samples in stage I, 1,500 cells from 2 samples in stage III, and 3,053 cells from 7 samples in stage IV (Figure 4A). We noticed that these scRNA-seq data sets contain batch effects across all stages (Figure S11A), presumably due to the multiple samples involved across multiple time points (iLISI = 0.10). Therefore, we performed both versions of TDEseq in such a scenario.

To do so, we first examined the ability of temporal gene detection methods in terms of type I error. As we expected, when batch effects exist, Mixed TDEseq produced the well-calibrated *p*-values, whereas Linear TDEseq generated the slightly inflated *p*-values. The other two methods tradeSeq and ImpulseDE2 generated much inflated *p*-values (Figure 4B). In terms of temporal expression gene detection, both versions of TDEseq outperformed other methods across a range of FDR cutoffs (Figure 4C). Specifically, Mixed TDEseq identified a total of 11,919 temporally expressed genes at an FDR of 5%, which were displayed four temporal distinct patterns (Figure 4D), while Linear TDEseq detected 12,263 temporal genes, tradeSeq detected 9,562 temporal genes and ImpulseDE2 identified 8,440 temporal genes (Table S4).

To validate whether the temporal expression genes were identified through methods related to epithelial cell evaluation, we performed the following two-line analyses. On the one hand, we curated a total of 136 LUAD-related genes from the ONGene database [65] (Table S5) to highlight the importance of temporal expression genes detected by different methods. As a result, we found that both versions of TDEseq enriched more genes than tradeSeq and ImpulseDE2 across a range of top genes (Figure 4E). On the other hand, we recruited a 3,040 LUAD-associated gene list from the TCGA database [66] (Table S5). As a result, we again

found that both versions of TDEseq enriched more genes than tradeSeq and ImpulseDE2 across a range of top genes (Figure 4F). In addition, we examined the temporal expression genes detected by Mixed TDEseq but not detected by tradeSeq or ImpulseDE2, finding many genes were associated with LUAD evolution. For example, a LUAD driver *MAP2K1* [67] was detected by Mixed TDEseq as significant temporal expression genes that gradually up-regulated during LUAD progression (*p*-value = 1.17e-7, FDR = 0), while not detected by ImpulseDE2 (*p*-value = 0.553, FDR = 0.105); Besides, another LUAD drivers *KRAS* [67] was also detected by Mixed TDEseq as significant temporal expression genes that gradually up-regulated during LUAD progression (*p*-value = 4.05e-12, FDR = 0), while not detected by tradeSeq (*p*-value = 0.089, FDR = 0.356). Furthermore, the Mixed TDEseq unique temporal expression genes were enriched in GO terms that related to the LUAD progression (Figure 4G), such as signal transduction by p53 class mediator [68] (GO:0072331; BH-adjusted *p*-value = 8.50e-6) and response to hypoxia [69] (GO:0001666; BH-adjusted *p*-value = 4.84e-3). Notably, though Linear TDEseq detected more temporal genes, the temporal genes uniquely identified by Mixed TDEseq were enriched in more biologically meaningful GO terms (Figure S11B), e.g., epithelial cell migration (GO:0010631; BH-adjusted *p*-value = 0.048).

Finally, we performed GSEA on the pattern-specific temporal expression genes to examine the four pattern-specific functions during LUAD progression. Specifically, with an FDR of 5%, Mixed TDEseq detected a total of 3,249 growth-specific temporal expression genes, which were enriched in 812 GO terms (Figure 4H). The top GO terms contained many tumor proliferation or metastasis-associated pathways, such as signal transduction by p53 class mediator [68] (GO:0072331; BH-adjusted *p*-value = 1.57e-6), regulation of canonical Wnt signaling pathway [70] (GO:0060828; BH-adjusted *p*-value = 2.81e-3), suggesting epithelial cells proliferation towards tumor cells; Mixed TDEseq identified a total of 3,671 recession-specific temporal expression genes, which were enriched in 276 GO terms (Figure 4H). Those genes would be expected enriched in normal lung function terms as a result of the process of low-grade tumors developing into high grade tumors. Indeed, the top GO terms contained lung development (GO:0030324; BH-adjusted *p*-value = 8.26e-3) and lamellar body (GO:0042599; BH-adjusted *p*-value = 4.08e-4), suggesting the proliferation process of epithelial cells towards tumor cells. TDEseq detected a total of 2,526 peak-specific temporal genes, which were enriched in a total of 244 GO terms. Notably, those peak genes

were further enriched in hypoxia pathways, such as response to oxidative stress (GO:0006979; BH-adjusted *p*-value = 1.19e-2), as well as epithelium migration (GO:0090132; BH-adjusted *p*-value = 4.56e-2). This evidence further validated the fact that the hypoxia occur in the intermediate stages of LUAD promoting lymphatic metastasis [69].

Taken together, Mixed TDEseq can address time-course scRNA-seq data with relatively large batch effects over multiple time points. However, one of the concerns regarding whether batch effects removal can improve the identification of temporal expression genes. To do so, we performed the temporal gene detection analysis using Mixed TDEseq either with or without batch correction. We found that Mixed TDEseq can generate well-calibrated *p*-values in both cases (Figure S11C). In terms of temporal expression gene detection, Mixed TDEseq alone would produce a more powerful performance than that with batch correction across a range of FDR cutoffs (Figure S11D). The slightly poor performance of Mixed TDEseq coupled with scMerge may be due to the over-correction. Furthermore, we observed the temporal expression genes uniquely identified by Mixed TDEseq were significantly enriched in LUAD-related pathways (Figure S11E), suggesting Mixed TDEseq well-addressed time-course scRNA-seq data with relatively large batch effects.

TDEseq detects NK cell response temporal genes of time-course scRNA-seq data

We finally applied TDEseq to detect the temporal expression changes of natural killer (NK) cells from 21 serve/critical COVID-19 patients [9]. This time-course scRNA-seq data set contains 19 time points (Materials and Methods; Table S1), which could be grouped into five developmental stages, i.e., stage I (consisting of 930 cells from 3 patients), stage II (939 cells from 4 patients), stage III (893 cells from 3 patients), stage IV (768 cells from 3 patients), stage V (1,000 cells from 8 patients). Since these scRNAseq data sets contain batch effects across different stages (Figure 5A), presumably due to the large number of heterogeneous patients involved in this study (iLISI = 0.11; Figure 5B). To do so, following the results from simulation studies, we first carried out Mixed TDEseq with or without the batch effect removal procedure using scMerge [51].

As we expected, in terms of type I error control, Mixed TDEseq, and Mixed TDEseq coupled with scMerge (Mixed TDEseq+scMerge) can produce well-calibrated *p*-values (Figure 5C). Besides, in terms of temporal gene detection, Mixed TDEseq

coupled with scMerge detected more temporal expression genes than Mixed TDEseq across a range of FDR cutoffs (Figure 5D), which were displayed four temporal distinct patterns (Figure 5E). Moreover, the temporal expression genes that uniquely detected by Mixed TDEseq+scMerge were more enriched in the defense response to the virus GO term (GO:0051607) [71] (Table S7; Figure 5F). Therefore, we performed the Mixed TDEseq with batch correction in the following analysis. The tradeSeq and ImpulseDE2 have originally built-in variables to control batch effects. For a fair comparison, we additionally incorporated the sample indicator variables as covariates in both tradeSeq and ImpulseDE2 models.

Notably, after accounting for batch effects as covariates included in the model, though tradeSeq and ImpulseDE2 generated *p*-values similar as the small batch effects scRNA-seq data (Figure 5C), tradeSeq only detected 244 temporal genes, and ImpluseDE2 only identified 3 temporal gene (Figure 5D; Table S4). Moreover, the temporal expression genes detected by Mixed TDEseq coupled with scMerge were significantly enriched in a gene set that is more specific to defense response to the virus GO term (GO:0051607) [71] (Table S7; Figure 5F). Many top temporal expression genes uniquely detected by Mixed TDEseq coupled with scMerge were highly related to the NK cell response to COVID-19 infection (Figure 5H). For example, an IFN-related genes *IFI6* that are highly expressed in NK cells in severe COVID-19 at the early stage [72] was identified by Mixed TDEseq coupled with scMerge as the top-ranked significant temporal expression gene (*p*-value = 3.60e-7, FDR = 0; Figure 5G), while was not detected by tradeSeq(*p*-value = 0.258, FDR = 1) and ImpulseDE2 (*p*-value = 0.982, FDR = 0.947). Another example is the *IFI35* gene which plays an important role in type I interferon generation during early SARS-COV-2 response [73], which was identified by Mixed TDEseq+scMerge (*p*-value = 3.77e-5, FDR = 0; Figure 5G) but did not detect by tradeSeq (*p*-value = 6.56e-3, FDR = 0.172) and ImpulseDE2 (*p*-value = 1, FDR = 1). This evidence supported that the temporal DE genes detected by Mixed TDEseq+scMerge were more specific to the SARS-COV-2 response biological process. Consequently, we further performed the GSEA on the temporal expression genes uniquely detected by Mixed TDEseq+scMerge, enriched in the immune response to virus infection pathways such as response to the virus (GO:0009615; BH-adjusted *p*-value = 7.63e-11), and type I interferon (GO:0034340; BH-adjusted *p*-value = 2.95e-10) [74] (Figure 5H).

Finally, we performed GSEA on the pattern-specific temporal expression genes.

Specifically, with an FDR of 5%, Mixed TDEseq+scMerge detected a total of 654 growth-specific temporal expression genes, which were significantly enriched in cell cycle-associated pathways (Figure 5I), such as mitotic G1/S transition checkpoint (GO:0044819; BH-adjusted *p*-value = 7.81e-3). It was shown that NK cells showcased up-regulated patterns of cell cycle and division after SARS-COV-2 infection [75]; also enriched in the cellular response to interleukin-12 (GO:0071349; BH-adjusted *p*-value = 1.33e-2), because IL-12 promotes NK cell proliferation at the end stage of SARS-COV-2 infection [76]; Mixed TDEseq+ scMerge detected a total of 809 recession-specific temporal expression genes, which were enriched in the immune response to the virus as a result of SARS-COV-2 infection (Figure 5I). Indeed, most of the top GO terms were immune response-associated pathways, such as defense response to the virus (GO:0051607; BH-adjusted *p*-value = 1.76e-29) and type I interferon signaling pathway (GO:0060337; BH-adjusted *p*-value = 1.81e-28) which promotes NK cell expansion during viral infection [77]; Mixed TDEseq+scMerge detected a total of 567 peak-specific temporal expression genes, which were enriched in oxidative phosphorylation (GO:0006119; BH-adjusted *p*-value = 0.025) and mitochondrial gene expression (GO:0140053; BH-adjusted *p*-value = 4.11e-2), consistent with that long period of activation enhances effector functions in the NK cells and upregulated OXPHOS [78, 79] (Figure 5I).

Taken together, we found Mixed TDEseq coupled with scMerge performs effectively in mitigating substantial batch effects present in time-course scRNA-seq data. However, the batch correction methods do introduce extra variations into the data. Therefore, a more comprehensive assessment of the performance of temporal gene testing is required to determine whether these variations are advantageous, particularly for sparse scRNA-seq data [33].

DISCUSSION

In this paper, we have presented TDEseq, a non-parametric statistical method designed for identifying temporal expression genes in time-resolved and time-course single-cell RNA sequencing (scRNA-seq) data. Two versions of TDEseq were developed to admit different real data application scenarios. By incorporating shape-constrained spline models, TDEseq typically enables the detection of four specific temporal patterns, i.e., growth, recession, peak, or trough. With extensive simulations and four real data applications, TDEseq generated well-calibrated *p*-values and demonstrated powerful detection of temporal expression genes, highlighting its robustness and reliability in time-resolved and time-course scRNA-seq data analysis.

Particularly, the statistical modeling of TDEseq is different from tradeSeq and ImpluseDE2. TDEseq and tradeSeq are two different methods used to model temporal expression patterns of time-resolved and time-course scRNA-seq data. TDEseq incorporates either *I*-splines [39] or *C*-splines [40] to model temporal expression patterns, and builds upon linear additive mixed models (Materials and Methods) to characterize the dependent cells within an individual. In contrast, tradeSeq [35] employs a generalized additive model framework to model gene expression profiles of pseudotime for different lineages; while ImpluseDE2 [29] relies on a descriptive impulse function[80] to distinguish permanently from transiently up- or down-regulated genes over multiple time points. In our study, we observed that the *p*-values from tradeSeq and ImpluseDE2 under permuted null were not well-calibrated even control the batch effects as covariates (Figure S6), presumably due to its inability to model dependent cells within an individual rather than independent cells. We also found that the power of tradeSeq or ImpluseDE2 was lower than TDEseq (Figure S2), likely due to its suitability for detecting a distinct type of differential expression patterns along a lineage or between lineages.

Based on the aforementioned observation, batch effects play a crucial role in the identification of temporal expression genes. However, the removal of batch effects in time-course scRNA-seq data poses significant challenges [81, 82], and there are currently no efficient criteria to measure these effects. Fortunately, we provide a solution called TDEseq, which can effectively handle such batch effects across multiple time points in time-course scRNA-seq studies. In contrast, tradeSeq and ImpluseDE2 directly model gene expression raw counts and incorporate the covariates to control the batch effects. However, this approach leads to a

significant loss in power for detecting temporal expression genes and inevitably increases the computational burden. This is why TDEseq was designed to model the transformed gene expression level rather than raw gene expression counts, allowing for scRNA-seq data preprocessing prior to performing temporal expression gene detection. Furthermore, even in the presence of large batch effects in scRNA-seq data, TDEseq, when coupled with batch removal methods, offers a promising approach to identifying temporal expression genes. In this study, we evaluated five batch removal methods, which returned batch-corrected expression matrices. The results indicated that scMerge display powerful performance than the other four methods. However, it is worth noting that the simulated scRNA-seq data may not fully mimic real-world scRNA-seq data. Therefore, alternative batch removal methods could also be applied to TDEseq analysis, especially a well-designed batch correction method specifically tailored for time-course scRNA-seq data, which would greatly enhance the performance of TDEseq.

Finally, several potential extensions for TDEseq can enhance its capabilities. Currently, TDEseq is limited to detecting four specific patterns (i.e., growth, recession, peak, and trough), which may result in missing accurate critical change points or tipping points at specific time points. Therefore, an improvement would be to successfully detect these shapes or critical points, as they would provide valuable biological insights. Furthermore, the parameter inference of LAMM, the underlying model of TDEseq, becomes notably challenging when the number of cells is large (sample size > 6,000). To address this issue, it would be beneficial to incorporate more efficient algorithms that reduce the computation burden. Alternatively, a down-sampling strategy or a pseudo-cell [2, 83] strategy could be employed for each time point when dealing with extremely large sample sizes.

Overall, TDEseq is well-suited to analyzing time-resolved and time-course scRNA-seq data sets. Thus, it can be flexibly deployed to investigate the important marker genes and their potential roles during a growth, development, or disease progression process.

MATERIALS AND METHODS

Models and Algorithm

As the aforementioned overview, TDEseq typically models the transformed gene expression levels along the multiple time points as inputs. Subsequently, TDEseq was performed to identify temporal expression genes that display one of four possible patterns (i.e., growth, recession, peak, or trough). Specifically, we assume the transformed gene expression level y_{gi} for gene g, individual j and cell i at stage t is,

$$y_{gji} = \boldsymbol{w}_{gji}\boldsymbol{\alpha}_g + \sum_{k=1}^{K} s_k(t)\beta_{gk} + u_{gj} + e_{gji},\ i = 1,2,\cdots,N; g = 1,2,\cdots,G; t = 1,2,\cdots,T, j = 1,\dots,M. \quad (1)$$

where $s_k(t)$ is a smoothing spline basis function to characterize the temporal gene expression patterns. The regression function is estimated by a linear combination of the basis function with constrained. In particular, the *I*-splines defined as $I_l^k(x) = \int_{\xi_1}^{x} M_l^k(v)dv$ [39] were used to characterize both growth and recession patterns; while *C*-splines as $C_l^k(x) = \int_{\xi_1}^{x} I_l^k(v)d(v)$ [40] taking integral operation of *I*-splines, were used to characterize both peak and trough patterns, where the order 1 *M*-splines are computed as,

$$M_l^1(x) = \begin{cases} \frac{1}{\xi_{l+1}-\xi_l}, & \xi_l \le x \le \xi_{l+1} \\ 0, & otherwise \end{cases}.$$

The order *k M*-splines are computed as

$$M_l^k(x) = \begin{cases} \frac{k[(x-\xi_l)M_l^{k-1}(x)+(\xi_{l+k}-x)M_{l+1}^{k-1}(x)]}{(k-1)(\xi_{l+k}-\xi_l)}, & \xi_l \le x \le \xi_{l+1} \\ 0, & otherwise \end{cases}.$$

where the number of *M*-splines basis functions is $k + l$; l is the number of grid points; k is the order of splines; we define knots $x_1 = \xi_1 < \cdots < \xi_{k+l} = x_n$. With the spline functions $s_1(t), \dots, s_K(t)$, we infer the parameters of Equation 1 for gene g, which could be translated into estimating the parameters of the equation,

$$\mathbf{E}(\boldsymbol{y}_g) = \mathbf{W}\boldsymbol{\alpha}_g + [\mathbf{W}_0\ \ \mathbf{S}][\begin{matrix}\boldsymbol{\alpha}_{g0} \\ \boldsymbol{\beta}_g\end{matrix}].$$

where $\mathbf{W}_0$ is the linear part of the spline basis function and $\mathbf{S}$ is the nonlinear part of the spline basis function which is an $n \times (k + l)$ matrix with columns $s_1(t), \dots, s_{k+l}(t)$, k is the number of knots of the spline functions; For the growth or recession patterns, $\mathbf{S}$ was assigned by *I*-spline basis functions and $\mathbf{W}_0 = \mathbf{I}_n$. For both peak and trough patterns, $\mathbf{S}$ was assigned by the *C*-spline basis vectors and $\mathbf{W}_0 = [\mathbf{I}_n, \boldsymbol{t}]$, where $\boldsymbol{t} = t_1, \dots, t_n$ represents the time points. $\mathbf{W}$ is a covariates matrix; $\boldsymbol{\alpha}_g$, $\boldsymbol{\alpha}_{g0}$ and $\boldsymbol{\beta}_g$ are the corresponding regression coefficients.

Hence, the complete likelihood $\boldsymbol{L}(\boldsymbol{y}_g, \boldsymbol{t}, \mathbf{W_0}, \mathbf{W} | \boldsymbol{\alpha}_{g0}, \boldsymbol{\alpha}_g, \boldsymbol{\beta}_g)$ of the transformed gene expression data $\boldsymbol{y}_g$ for gene g at a time, $\boldsymbol{t}$ is:

$$\boldsymbol{L}\left(\boldsymbol{y}_g, \boldsymbol{t}, \mathbf{W_0}, \mathbf{W} \middle| \boldsymbol{\alpha}_{g0}, \boldsymbol{\alpha}_g, \boldsymbol{\beta}_g\right) = MVN(\boldsymbol{\mu}_g, \sigma_g^2 \mathbf{K}_g).$$

where $\boldsymbol{\mu}_g = \mathbf{E}(\boldsymbol{y}_g) = \mathbf{W}_0 \boldsymbol{\alpha}_{g0} + \mathbf{W} \boldsymbol{\alpha}_g + \mathbf{S} \boldsymbol{\beta}_g$ is the mean and $\mathbf{K}_g = \frac{\sigma_{gu}^2}{\sigma_g^2} \boldsymbol{\Sigma}_{r \times r} + \mathbf{I}_{r \times r}$ is the covariance matrix; $MVN(\cdot)$ represents multivariate normal distribution. For any pattern constraints, we assume a linearly independent set of $\mathbf{S}, \mathbf{W}_0$ and $\mathbf{W}$ together as a closed convex cone:

$$\nabla = \left\{ \boldsymbol{\mu}_g \in \mathbb{R}^n : \boldsymbol{\mu}_g = \mathbf{E}\left(\boldsymbol{y}_g(t)\right) = \mathbf{W}_0 \boldsymbol{\alpha}_{g0} + \mathbf{W} \boldsymbol{\alpha}_g + \mathbf{S} \boldsymbol{\beta}_g, \boldsymbol{\beta}_g \geq 0 \right\}. \quad (2)$$

The parameter estimation of TDEseq models is notoriously difficult, as it involves the calculation of a matrix determinant and a matrix inversion of $\mathbf{K}_g$. To enable scalable estimation and inference for TDEseq models, we have developed an efficient inference algorithm that: 1) performs a block diagonal matrix (one individual as an all-one block matrix) eigen-decomposition (Supplementary Text), i.e., $\mathbf{K}_g = \frac{\sigma_{gu}^2}{\sigma_g^2} \boldsymbol{\Sigma}_{r \times r} + \mathbf{I}_{r \times r} = \mathbf{U}_g \mathbf{U}_g^{\boldsymbol{T}}$; 2) transforms the variables of Equation 2 as: $\widetilde{\boldsymbol{y}}_g = \mathbf{U}_g^{-1} \boldsymbol{y}_g, \widetilde{\mathbf{W}}_0 = \mathbf{U}_g^{-1} \mathbf{W}_0, \widetilde{\mathbf{W}} = \mathbf{U}_g^{-1} \mathbf{W}$, and, $\tilde{\mathbf{S}} = \mathbf{U}_g^{-1} \mathbf{S}$ resulting in

$$\mathbf{E}\left(\widetilde{\boldsymbol{y}}_g(t)\right) = \widetilde{\mathbf{W}}_0 \boldsymbol{\alpha}_{g0} + \widetilde{\mathbf{W}} \boldsymbol{\alpha}_g + \tilde{\mathbf{S}} \boldsymbol{\beta}_g. \quad (3)$$

and the following new closed convex cone:

$$\nabla = \left\{ \widetilde{\boldsymbol{\mu}}_g \in \mathbb{R}^n : \widetilde{\boldsymbol{\mu}}_g = \widetilde{\mathbf{W}}_0 \boldsymbol{\alpha}_{g0} + \widetilde{\mathbf{W}} \boldsymbol{\alpha}_g + \tilde{\mathbf{S}} \boldsymbol{\beta}_g, \boldsymbol{\beta}_g \geq 0 \right\}. \quad (4)$$

To efficiently estimate the parameter of an ordinary linear regression model (Equation 3) with cone constraint (Equation 4), we developed a cone projection algorithm following previous work [44]. With the estimated parameters, we further examined the gene expression pattern-specific parameter $\boldsymbol{\beta}_g$, which follows a mixture of *Beta* distributions [84] (Supplementary Text). Finally, TDEseq returns *p*-values for four temporal expression patterns, i.e., growth, recession, peak, and trough.

The choice of parameter knots in TDEseq models

The number of knots can significantly influence the smoothness and flexibility of the resulting curve [85]. Increasing the number of knots in general results in a more adaptable spline, enhancing its ability to capture intricate and irregular data patterns. Nonetheless, excessive flexibility in a spline can lead to overfitting,

causing it to closely mimic noise in the data instead of representing the fundamental trend. Conversely, using too few knots can lead to underfitting, resulting in an overly smooth spline that misses crucial data features. Particularly, in this paper, we found that temporal gene detections are typically more robust with varying the number of knots across a range of FDR cutoffs (Figure S12). TDEseq performed well when the number of knots *k* equals the number of time points. Therefore, we set the number of knots of TDEseq as the number of time points by default.

Linear TDEseq

Linear TDEseq is a reduced special model of Mixed TDEseq (Equation 1), which drops the random effect term $\boldsymbol{u}_{gi}(t)$, typically to model only one individual involved in each stage or small batch effects across all stages in time-resolved or time-course scRNA-seq data. Specifically, we assume the transformed gene expression level y_{gi} for gene g and cell i at stage t can be modeled as,

$$y_{gi} = \boldsymbol{w}_{gi}\boldsymbol{\alpha}_g + \sum_{k=1}^{K} s_k(t)\beta_{gk} + e_{gi},\ i = 1,2,\cdots,N; g = 1,2,\cdots,G; t = 1,2,\cdots,T \quad (5)$$

As a result, the parameter estimates of Equation 5 could fall into Equations 3 and 4, where the $\mathrm{cov}(\boldsymbol{y}_g) = \sigma_g^2\mathbf{I}_{N\times N}$. Therefore, we can directly apply the cone projection algorithm to estimate ($\boldsymbol{\alpha}_{g0}, \boldsymbol{\alpha}_g, \boldsymbol{\beta}_g, \sigma_g^2$) without iteration procedure. Compared with Mixed TDEseq, Linear TDEseq is much more efficient in large-scale time-resolved or time-course scRNA-seq data.

Testing temporal expression patterns

Testing whether a gene shows a temporal expression pattern over all time points can be translated into testing the null hypothesis: $\mathbf{H_0}: \boldsymbol{\beta}_g = 0$. The statistical power of such a hypothesis test will depend on how well the pattern-constrained spline function fits the observed temporal expressions. We, therefore, compute *p*-values for growth, recession, peak, or trough (each at a time), thereby combining these four *p*-values through the Cauchy combination rule [47]. Specifically, we first convert each of the four *p*-values into a Cauchy statistic, and then aggregate the four Cauchy statistics through summation and convert the summation back to a single *p*-value based on the standard Cauchy distribution (Supplementary Text). After obtaining *m p*-values across *m* genes, we computed the false discovery rate (FDR) through the permutation strategy.

Determining one of the temporal expression patterns for each gene

A primary goal of TDEseq is assigning a suitable expression pattern of four given patterns (i.e., growth, recession, peak, or trough) for each gene. Specifically, for the linear version of TDEseq, TDEseq calculated the *Akaike* information criterion (AIC) [86] for gene g:

$$AIC_{gp} = 2k + nlog(L_{gp}), \qquad p = 1, 2, 3, or\ 4.$$

where *k* is the number of parameters and L_{gp} is the likelihood for gene g and pattern p. For Mixed TDEseq, the marginal AIC is not an asymptotically unbiased estimator of the AIC and favors smaller models without random effects, but conditional AIC induces a bias that can lead to the selection of any random effect not predicted to be exactly zero [87]. Therefore, we used *B*-statistics to determine the temporal expression patterns for gene g:

$$B_{gp} = \frac{SSR_{gp0} - SSR_{gp1}}{SSR_{gp0}}, \qquad p = 1, 2, 3, or\ 4.$$

Where SSR_{gp1} is the sum of squared residuals with parameters estimated via cone projection algorithm, and SSR_{gp0} is the sum of squared residuals under the null hypothesis.

Simulations

To make our simulations as realistic as possible, we simulated time-course scRNA-seq data using the *Splatter* package[48], in which the parameters were inferred from real LUAD scRNA-seq data. Our strategy involved creating a baseline dataset as the initial time point and sequentially generating datasets for each adjacent time point. The expression levels of differentially expressed genes (i.e., temporal expression genes) between consecutive stages were modified based on fold change parameters (*de.facloc*). Specifically, in null simulations, we set the probability of the differential expression genes *de.prob* = 0 and the effect of consecutive stage parameter *de.facloc* = 0 to denote the non-temporal expression gene across all multiple stages. We simulated 200 cells measured by 10,000 genes for each stage to examine the performance of type I error control.

In power simulations, we varied the numbers of time points, sample sizes, the effect of consecutive stage parameter *de.facloc*, and expected UMI counts *lib.loc*. To do so, we set the probability of a gene being temporal expression in a group *de.prob* = 0.3, the number of stages as 5, the effect of consecutive stage parameter *de.facloc* = 0.4, and expected UMI counts *lib.loc* = 9.4 as the baseline simulation scenario. We then varied the number of stages to be either 4, 5, or 6 (300 cells for each stage); the number of cells to be either 100, 200, or 300 for each stage; the effect of consecutive stage parameter as 0.1, 0.4 or 0.7; expected UMI counts as

7, 9.4 and 13.7 (estimates from rat liver scRNA-seq data). For the batch effects, we simulated 100 cells for each batch, and we varied batch effects among individuals to 0%, 10%, or 30% differential expressed factors (i.e., set *batch.facloc* as 0, 0.04, or 0.12) to represent small, moderate or strong batch effect sizes. We restricted the temporal expression genes that exhibit growth, recession, peak, or trough patterns. We repeated 10 times for each simulation scenario.

The difference in statistical models among TDEseq and tradeSeq or ImpluseDE2

In addition to TDEseq, we also employed other two temporal expression analysis methods, tradeSeq, and ImpulseDE2. The tradeSeq builds on the generalized additive model (GAM) that directly models raw gene expression counts in scRNA-seq data, i.e.,

$$y_{gi} \sim NB(\mu_{gi}, \phi_g)$$

$$\log(\mu_{gi}) = \boldsymbol{w}_i \boldsymbol{\alpha}_g + \sum_{k=1}^{K} b_k(t)\beta_{gk} + log\ (N_i)$$

where y_{gi} represents the raw counts for gene g and cell i; t represents the time points; $\boldsymbol{w}_{gi}$ represents the covariates and $\sum_{k=1}^{K} b_k(t)\beta_{gk}$ represents a linear combination of K cubic basis functions; T_i denotes the total counts for cell i; NB is a negative binomial distribution. To avoid overfitting issues, tradeSeq employed penalized spline which shrinkages β_{gk} to zero, and therefore are less sensitive to temporal genes with small fold changes. Notably, tradeSeq [49] was primarily developed for detecting trajectory-based differential expression genes, however, the applicability of tradeSeq was extended beyond this setting, i.e., also can be applied to bulk time-course RNA-seq data analysis [35]. Therefore, we performed an analogous analysis using tradeSeq in the comparison. On the other hand, ImpulseDE2 [29] combines the impulse model [80] with a negative binomial noise model to directly model the raw counts of gene expression measurements. The impulse function is the scaled product of two sigmoid functions:

$$\mu(t) = f_{Impulse}(t) = \frac{1}{h_1}\left(h_0 + (h_1 - h_0)\frac{1}{1 + e^{-\beta(t-t_1)}}\right) * (h_2 + (h_1 - h_2)\frac{1}{1 + e^{\beta(t-t_2)}}$$

where $h_0 = f_{Impulse}(t \to -\infty), h_2 = f_{Impulse}(t \to \infty)$ and h_1 models the intermediate expression, t_1 and t_2 are the state transition times, β is the slope parameter of both sigmoid functions.

The impulse function is a more restrictive model compared with spline functions, therefore limiting its power. It was originally designed to model the bulk time-course RNA-seq data. To adapt for temporal expression analysis of time-course scRNA-

seq data, we modified the implementation of ImpulseDE2 following the tradeSeq paper. Both methods take a count matrix ***Y*** and a time points vector ***t*** as input and return one *p*-value for each gene at a time.

Specifically, for tradeSeq (version 1.4.0), we use the functions *fitGAM* and *associationTest* (https://statomics.github.io/tradeSeq/articles/tradeSeq.html). The number of knots parameter *k* in the tradeSeq is chosen by 100 random genes based on tradeSeq vignette. For ImpulseDE2 (version 0.99.10), we follow the modified implementation of ImpulseDE2 in the tradeSeq paper (https://github.com/statOmics/tradeSeqPaper).

Permutation strategy to construct the null distribution

In real data applications, to calculate the false discovery rate (FDR), we construct an empirical null distribution of *p*-values through permuting the time point variables, and repeated 5 times. Afterward, we computed the FDRs using

$$fdr_g = \frac{\sum_{k=1}^{g}\sum_{r=1}^{5} I\left(P_g^{alt} > P_{rk}^{null}\right)}{5*g},\ g = 1,2,\cdots,G.$$

where P_{rk}^{null} is an increasing ordered *p*-value for k^{th} gene and r^{th} permutation; P_g^{alt} is an increasing ordered *p*-values under the alternative hypothesis.

Functional gene set enrichment analysis

The gene set enrichment analyses of temporal expression genes were performed by the *enrichGO* function implemented in the clusterProfiler R package (version 3.18.1) [88]. Specifically, we used all genes in scRNA-seq data were analyzed as the background, and set the minimal and maximal sizes of genes annotated by Gene Ontology term for testing as 10 and 500, respectively. The significant GO terms were selected with BH-adjusted *p*-value < 0.05.

Batch effects removal evaluation

We used the LISI metric to measure cell batch distribution (iLISI) [55]. The LISI metric is designed for assessing whether clusters of cells in a scRNA-seq dataset are well-mixed across categorical variables (batches). We took the median value of the scores computed for all cells in the dataset and scaled the value between 0 and 1 to denote the worst and best cell mixed.

HCT116 cell lines after 5-AZA-CdR treatment data

The scRNA-seq data were assayed by Well-TEMP-seq, which contains 5-AZA-CdR-treatment HCT116 cell lines after 0 day (4,000 cells), 1 day (4,000 cells), 2 days (4,000 cells) or 3 days (4,000 cells) [23]. The Well-TEMP-seq technology can

distinguish new RNAs from pre-existing RNAs, we used the new RNAs which better reflect RNA dynamics for downstream analysis. For the preprocessing of scRNA-seq data, the genes with more than 99% of zero counts were filtered out, resulting in 7,314 genes and 16,000 cells for further analysis.

Mouse hepatoblast differentiation data

The scRNA-seq data were assayed by Smart-seq2 protocols [61] on isolated cells from mouse fetal livers at 7 different developmental stages [41]. Gene expression levels were measured by a total of 14,226 genes and 345 cells. In our analysis, we only considered the hepatoblast cells for temporal expression analysis. Finally, for the preprocessing of scRNA-seq data, the genes with more than 99% of zero counts were filtered out, resulting in 14,180 genes and 345 cells for further analysis.

Human metastatic LUAD progression data

The scRNA-seq data [14] were assayed by 10X Genomics Chromium protocols [89] on LUAD samples from 5 distinct developmental stages, i.e., the control stage consists of a total of 80,441 cells in 7 cell types from 21 samples; stage I consists of a total of 31,026 cells in 7 cell types from 8 samples; stage II consists of a total of 3,840 cells in 7 cell types from 1 sample, stage III consists of a total of 10,283 cells in 7 cell types from 2 samples, and stage IV (metastasis) consists of a total of 82,916 cells in 7 cell types from 26 samples. In our analysis, we only employed the epithelial cells from the control lung samples (3,703 cells), stage I tumor lung samples (5,651 cells), stage III tumor lung samples (1,500 cells), and stage IV samples (lymph node metastasis, 6,582 cells). To relieve the computational burden in practice, we utilized a down sampling strategery to randomly select 1,000 cells for the stage that contains more than 1,000 cells. Finally, for the preprocessing of scRNA-seq data, the genes with more than 99% of zero counts were filtered out, resulting in 15,263 genes and 4,000 cells for further analysis.

Human COVID-19 immune response data

This scRNA-seq data were assayed by 10X Genomics Chromium protocols on human SARS-COV-2 infection samples from disease progression ranging from 4 days to 123 days [9]. In our analysis, we only employed the NK cells from the 21 serve/critical patients and divided those patients into 5 stages according to the time point interval, i.e. stage I (4-8 days, 930 cells), stage II (10-13days, 939 cells), stage III (19-24 days, 893 cells), stage IV (28-34days, 768 cells) and stage V (110-123days, 1,000 cells). Finally, for the preprocessing of scRNA-seq data, the genes with more than 99% of zero counts were filtered out, resulting in 10,699 genes and 4,530 cells for further analysis.

AVAILABILITY OF DATA AND CODE

All scRNA-seq data sets used in this study are publicly available on the GEO database. Specifically, mouse hepatoblast differentiation scRNA-seq data are available at GEO under accession GSE90047; Human metastatic LUAD progression scRNA-seq data are available at GEO under accession GSE131907; Human COVID-19 immune response scRNA-seq data are available at GEO under accession GSE158055. Well-TEMP-seq scRNA-seq data are available at GEO under accession GSE194357. The R package and web server of TDEseq is publicly available at https://sqsun.github.io/software.html. The source code and scRNA-seq data for reproducing the results are publicly available at https://sqsun.github.io/software.html.

ACKNOWLEDGEMENTS

This study was supported by the STI2030-Major Project (Grant No. 2022ZD0208000) to SS, LL, and YF; the National Natural Science Foundation of China (Grant Nos. 82122061 and 61902319) to SS; the National Natural Science Foundation of China (Grant No. 82204173) and the Natural Science Foundation of Shaanxi Province (Grant No. 2022JQ-773) to YF.

CONTRIBUTIONS

SS conceived the idea of the manuscript and provided funding support. SS and YF developed the method and designed the experiments. YF implemented the software and performed simulations and real data analysis with assistance from LL. SS and YF wrote the manuscript. All authors approved the final manuscript.

COMPETING INTERESTS

The authors declare no conflict of interests.

REFERENCE

1. Qiu, Q., et al., *Massively parallel and time-resolved RNA sequencing in single cells with scNT-seq.* Nature Methods, 2020. **17**(10): p. 991-1001.
2. Han, X.P., et al., *Construction of a human cell landscape at single-cell level.* Nature, 2020. **581**(7808): p. 303-309.
3. Chen, W., et al., *Live-seq enables temporal transcriptomic recording of single cells.* Nature, 2022. **608**(7924): p. 733-740.
4. Saelens, W., et al., *A comparison of single-cell trajectory inference methods.* Nat Biotechnol, 2019. **37**(5): p. 547-554.
5. Qiu, X., et al., *Reversed graph embedding resolves complex single-cell trajectories.* Nat Methods, 2017. **14**(10): p. 979-982.
6. Street, K., et al., *Slingshot: cell lineage and pseudotime inference for single-cell transcriptomics.* BMC Genomics, 2018. **19**(1): p. 477.
7. Cao, J.Y., et al., *Sci-fate characterizes the dynamics of gene expression in single cells.* Nature Biotechnology, 2020. **38**(8): p. 980-988.
8. Hu, F., J. Warren, and D.J. Exeter, *Interrupted time series analysis on first cardiovascular disease hospitalization for adherence to lipid-lowering therapy.* Pharmacoepidemiol Drug Saf, 2020. **29**(2): p. 150-160.
9. Ren, X., et al., *COVID-19 immune features revealed by a large-scale single-cell transcriptome atlas.* Cell, 2021. **184**(7): p. 1895-1913 e19.
10. Garcia-Alonso, L., et al., *Single-cell roadmap of human gonadal development.* Nature, 2022. **607**(7919): p. 540-547.
11. Fan, X.Y., et al., *Single-cell transcriptome analysis reveals cell lineage specification in temporal-spatial patterns in human cortical development.* Science Advances, 2020. **6**(34): p. eaaz2978.
12. Zhu, J., et al., *Delineating the dynamic evolution from preneoplasia to invasive lung adenocarcinoma by integrating single-cell RNA sequencing and spatial transcriptomics.* Exp Mol Med, 2022. **54**(11): p. 2060-2076.
13. Wang, Z., et al., *Deciphering cell lineage specification of human lung adenocarcinoma with single-cell RNA sequencing.* Nature communications, 2021. **12**(1): p. 1-15.
14. Kim, N., et al., *Single-cell RNA sequencing demonstrates the molecular and cellular reprogramming of metastatic lung adenocarcinoma.* Nature Communications, 2020. **11**(1): p. 2285.
15. Zou, Z.R., et al., *A Single-Cell Transcriptomic Atlas of Human Skin Aging.* Developmental Cell, 2021. **56**(3): p. 383-397.
16. Mogilenko, D.A., I. Shchukina, and M.N. Artyomov, *Immune ageing at single-cell resolution.* Nature Reviews Immunology, 2022. **22**(8): p. 484-498.
17. Allen, W.E., et al., *Molecular and spatial signatures of mouse brain aging at single-cell resolution.* Cell, 2023. **186**(1): p. 194-208.
18. Su, X., et al., *Single-cell RNA-Seq analysis reveals dynamic trajectories during mouse liver development.* BMC Genomics, 2017. **18**(1): p. 946.

19. Shao, L., et al., *Identify differential genes and cell subclusters from time-series scRNA-seq data using scTITANS.* Comput Struct Biotechnol J, 2021. **19**: p. 4132-4141.
20. Ding, J., N. Sharon, and Z. Bar-Joseph, *Temporal modelling using single-cell transcriptomics.* Nature Reviews Genetics, 2022. **23**(6): p. 355-368.
21. Bar-Joseph, Z., A. Gitter, and I. Simon, *STUDY DESIGNS Studying and modelling dynamic biological processes using time-series gene expression data.* Nature Reviews Genetics, 2012. **13**(8): p. 552-564.
22. Bar-Joseph, Z., *Analyzing time series gene expression data.* Bioinformatics, 2004. **20**(16): p. 2493-2503.
23. Lin, S., et al., *Well-TEMP-seq as a microwell-based strategy for massively parallel profiling of single-cell temporal RNA dynamics.* Nature Communications, 2023. **14**(1): p. 1272.
24. Gao, S., et al., *Tracing the temporal-spatial transcriptome landscapes of the human fetal digestive tract using single-cell RNA-sequencing.* Nature Cell Biology, 2018. **20**(6): p. 721-734.
25. Koenig, A.L., et al., *Single-cell transcriptomics reveals cell-type-specific diversification in human heart failure.* Nature Cardiovascular Research, 2022. **1**(3): p. 263-280.
26. Love, M.I., W. Huber, and S. Anders, *Moderated estimation of fold change and dispersion for RNA-seq data with DESeq2.* Genome Biol, 2014. **15**(12): p. 550.
27. Perez, R.K., et al., *Single-cell RNA-seq reveals cell type-specific molecular and genetic associations to lupus.* Science, 2022. **376**(6589): p. 153-165.
28. Robinson, M.D., D.J. McCarthy, and G.K. Smyth, *edgeR: a Bioconductor package for differential expression analysis of digital gene expression data.* Bioinformatics, 2010. **26**(1): p. 139-140.
29. Fischer, D.S., F.J. Theis, and N. Yosef, *Impulse model-based differential expression analysis of time course sequencing data.* Nucleic Acids Research, 2018. **46**(20): p. e119.
30. Conesa, A., et al., *maSigPro: a method to identify significantly differential expression profiles in time-course microarray experiments.* Bioinformatics, 2006. **22**(9): p. 1096-1102.
31. Nueda, M.J., S. Tarazona, and A. Conesa, *Next maSigPro: updating maSigPro bioconductor package for RNA-seq time series.* Bioinformatics, 2014. **30**(18): p. 2598-2602.
32. Lahnemann, D., et al., *Eleven grand challenges in single-cell data science.* Genome Biol, 2020. **21**(1): p. 31.
33. Nguyen, H.C.T., et al., *Benchmarking integration of single-cell differential expression.* Nature Communications, 2023. **14**(1): p. 1570.
34. Goldman, S.L., et al., *The Impact of Heterogeneity on Single-Cell Sequencing.* Frontiers in Genetics, 2019. **10**: p. 8.
35. Van den Berge, K., et al., *Trajectory-based differential expression analysis for single-cell sequencing data.* Nature Communications, 2020. **11**(1): p. 1-13.
36. Song, D.Y. and J.J. Li, *PseudotimeDE: inference of differential gene expression along cell pseudotime with well-calibrated p-values from single-cell RNA sequencing data.* Genome Biology, 2021. **22**(1): p. 124.
37. Lange, M., et al., *CellRank for directed single-cell fate mapping.* Nature Methods, 2022. **19**(2): p. 159-170.

38. Setty, M., et al., *Characterization of cell fate probabilities in single-cell data with Palantir.* Nature Biotechnology, 2019. **37**(4): p. 451-460.
39. Ramsay, J.O., *Monotone Regression Splines in Action.* Statistical Science, 1988. **3**(4): p. 425-441.
40. Meyer, M.C., *Inference Using Shape-Restricted Regression Splines.* Annals of Applied Statistics, 2008. **2**(3): p. 1013-1033.
41. Yang, L., et al., *A single-cell transcriptomic analysis reveals precise pathways and regulatory mechanisms underlying hepatoblast differentiation.* Hepatology, 2017. **66**(5): p. 1387-1401.
42. Chen, C., *Generalized additive mixed models.* Communications in Statistics-Theory and Methods, 2000. **29**(5-6): p. 1257-1271.
43. Curry, H.B. and I.J. Schoenberg, *On Pólya frequency functions IV: The fundamental spline functions and their limits.* Journal D'analyse Mathématique, 1966. **17**(1): p. 71-107.
44. Meyer, M.C., *A Simple New Algorithm for Quadratic Programming with Applications in Statistics.* Communications in Statistics-Simulation and Computation, 2013. **42**(5): p. 1126-1139.
45. Meyer, M.C., *A Test for Linear versus Convex Regression Function Using Shape-Restricted Regression.* Biometrika, 2003. **90**(1): p. 223-232.
46. Robertson, T., F.T. Wright, and R.L. Dykstra, *Order restricted statistical inference.* Journal of the American Statal Association, 1990. **85**(410).
47. Liu, Y.W., et al., *ACAT: A Fast and Powerful p Value Combination Method for Rare-Variant Analysis in Sequencing Studies.* American Journal of Human Genetics, 2019. **104**(3): p. 410-421.
48. Zappia, L., B. Phipson, and A. Oshlack, *Splatter: simulation of single-cell RNA sequencing data.* Genome Biology, 2017. **18**: p. 174.
49. Van den Berge, K., et al., *Trajectory-based differential expression analysis for single-cell sequencing data.* Nature Communications, 2020. **11**(1): p. 1201.
50. Haghverdi, L., et al., *Batch effects in single-cell RNA-sequencing data are corrected by matching mutual nearest neighbors.* Nat Biotechnol, 2018. **36**(5): p. 421-427.
51. Lin, Y., et al., *scMerge leverages factor analysis, stable expression, and pseudoreplication to merge multiple single-cell RNA-seq datasets.* Proceedings of the National Academy of Sciences, 2019. **116**(20): p. 9775-9784.
52. Risso, D., et al., *A general and flexible method for signal extraction from single-cell RNA-seq data.* Nat Commun, 2018. **9**(1): p. 284.
53. Johnson, W.E., C. Li, and A. Rabinovic, *Adjusting batch effects in microarray expression data using empirical Bayes methods.* Biostatistics, 2007. **8**(1): p. 118-127.
54. Smyth, G.K. and T. Speed, *Normalization of cDNA microarray data.* Methods, 2003. **31**(4): p. 265-273.
55. Tran, H.T.N., et al., *A benchmark of batch-effect correction methods for single-cell RNA sequencing data.* Genome Biol, 2020. **21**(1): p. 12.
56. Kocemba, K.A., et al., *Transcriptional silencing of the Wnt-antagonist DKK1 by promoter methylation is associated with enhanced Wnt signaling in advanced multiple myeloma.* PLoS

One, 2012. **7**(2): p. e30359.
57. Liu, M.M., et al., *Vitamin C increases viral mimicry induced by 5-aza-2 '-deoxycytidine.* Proceedings of the National Academy of Sciences of the United States of America, 2016. **113**(37): p. 10238-10244.
58. Roulois, D., et al., *DNA-Demethylating Agents Target Colorectal Cancer Cells by Inducing Viral Mimicry by Endogenous Transcripts.* Cell, 2015. **162**(5): p. 961-973.
59. Zheng, Y.C. and S.Q. Feng, *Epigenetic Modifications as Therapeutic Targets.* Current Drug Targets, 2020. **21**(11): p. 1046-1046.
60. Gleneadie, H.J., et al., *The anti-tumour activity of DNA methylation inhibitor 5-aza-2 '-deoxycytidine is enhanced by the common analgesic paracetamol through induction of oxidative stress.* Cancer Letters, 2021. **501**: p. 172-186.
61. Picelli, S., et al., *Smart-seq2 for sensitive full-length transcriptome profiling in single cells.* Nat Methods, 2013. **10**(11): p. 1096-1098.
62. Meng, Q., et al., *Repression of MAP3K1 expression and JNK activity by canonical Wnt signaling.* Dev Biol, 2018. **440**(2): p. 129-136.
63. Zhao, Y., et al., *ATF4 plays a pivotal role in the development of functional hematopoietic stem cells in mouse fetal liver.* Blood, 2015. **126**(21): p. 2383-2391.
64. Weninger, W.J., et al., *Phenotyping structural abnormalities in mouse embryos using high-resolution episcopic microscopy.* Dis Model Mech, 2014. **7**(10): p. 1143-1152.
65. Liu, Y.N., J.C. Sun, and M. Zhao, *ONGene: A literature-based database for human oncogenes.* Journal of Genetics and Genomics, 2017. **44**(2): p. 119-121.
66. Tang, G., M. Cho, and X. Wang, *OncoDB: an interactive online database for analysis of gene expression and viral infection in cancer.* Nucleic Acids Research, 2022. **50**(D1): p. D1334-D1339.
67. Pao, W. and N. Girard, *New driver mutations in non-small-cell lung cancer.* Lancet Oncology, 2011. **12**(2): p. 175-180.
68. Huang, J., *Current developments of targeting the p53 signaling pathway for cancer treatment.* Pharmacol Ther, 2021. **220**: p. 107720.
69. Muz, B., et al., *The role of hypoxia in cancer progression, angiogenesis, metastasis, and resistance to therapy.* Hypoxia (Auckl), 2015. **3**: p. 83-92.
70. Luo, J., et al., *PITX2 enhances progression of lung adenocarcinoma by transcriptionally regulating WNT3A and activating Wnt/beta-catenin signaling pathway.* Cancer Cell Int, 2019. **19**: p. 96.
71. Xie, Z., et al., *Gene Set Knowledge Discovery with Enrichr.* Curr Protoc, 2021. **1**(3): p. e90.
72. Kramer, B., et al., *Early IFN-alpha signatures and persistent dysfunction are distinguishing features of NK cells in severe COVID-19.* Immunity, 2021. **54**(11): p. 2650-2669 e14.
73. Ribero, M.S., et al., *Interplay between SARS-CoV-2 and the type I interferon response.* Plos Pathogens, 2020. **16**(7): p. e1008737.
74. Ouyang, W., et al., *Regulation and functions of the IL-10 family of cytokines in inflammation and disease.* Annu Rev Immunol, 2011. **29**: p. 71-109.
75. Cao, X., *COVID-19: immunopathology and its implications for therapy.* Nat Rev Immunol,

2020. **20**(5): p. 269-270.

76. Shemesh, A., et al., *Diminished cell proliferation promotes natural killer cell adaptive-like phenotype by limiting FcepsilonRIgamma expression.* J Exp Med, 2022. **219**(11): p. e20220551.
77. Madera, S., et al., *Type I IFN promotes NK cell expansion during viral infection by protecting NK cells against fratricide.* J Exp Med, 2016. **213**(2): p. 225-233.
78. Osuna-Espinoza, K.Y. and A.G. Rosas-Taraco, *Metabolism of NK cells during viral infections.* Front Immunol, 2023. **14**: p. 1064101.
79. Kumar, A., et al., *Enhanced oxidative phosphorylation in NKT cells is essential for their survival and function.* Proc Natl Acad Sci U S A, 2019. **116**(15): p. 7439-7448.
80. Gal, C. and K. Daphne, *Timing of Gene Expression Responses to Environmental Changes.* Journal of Computational Biology, 2009. **16**(2): p. 279-290.
81. Luecken, M.D., et al., *Benchmarking atlas-level data integration in single-cell genomics.* Nature Methods, 2022. **19**(1): p. 41-50.
82. Guo, X.Y., et al., *Recent advances in differential expression analysis for single-cell RNA-seq and spatially resolved transcriptomic studies.* Briefings in Functional Genomics, 2023: p. Early access.
83. You, Y., et al., *Modeling group heteroscedasticity in single-cell RNA-seq pseudo-bulk data.* Genome Biology, 2023. **24**(1): p. 107.
84. Nuesch, P.E., *Order Restricted Statistical-Inference - Robertson,T, Wright,Ft, Dykstra,Rl.* Journal of Applied Econometrics, 1991. **6**(1): p. 105-107.
85. Johs, B. and J.S. Hale, *Dielectric function representation by B-splines.* Physica Status Solidi a-Applications and Materials Science, 2008. **205**(4): p. 715-719.
86. Akaike, H., *Information Theory and an Extension of the Maximum Likelihood Principle.* Springer New York, 1998.
87. Greven, S. and T. Kneib, *On the behaviour of marginal and conditional AIC in linear mixed models.* Biometrika, 2010. **97**(4): p. 773-789.
88. Yu, G.C., et al., *clusterProfiler: an R Package for Comparing Biological Themes Among Gene Clusters.* Omics-a Journal Of Integrative Biology, 2012. **16**(5): p. 284-287.
89. Zheng, G.X., et al., *Massively parallel digital transcriptional profiling of single cells.* Nat Commun, 2017. **8**: p. 14049.

Figure 1. **Schematic overview of TDEseq and the methods comparison in simulations**. (**A**) TDEseq is designed to perform temporal expression gene analysis on time-resolved and time-course scRNA-seq data. With a given gene, TDEseq determines one of four temporal expression patterns, i.e., growth, recession, peak, and trough. TDEseq combines the four *p*-values using the Cauchy combination rule as a final *p*-value, facilitating the detection of one of four temporal gene expression patterns. (**B**) The quantile-quantile (QQ) plot shows the type I error control under the baseline parameter settings. The well-calibrated *p*-values will be expected laid on the diagonal line. The *p*-values generated from Mixed TDEseq (plum) are reasonably well-calibrated, while Linear TDEseq(orange), tradeSeq (green), ImpulseDE2 (blue), and Wilcoxon test (yellow) produced the *p*-values that are not well-calibrated. (**C**) The average power of 10 simulations for temporal expression gene detection across a range of FDR cutoffs under the baseline parameter settings. Both versions of TDEseq exhibit the high temporal expression gene detection power, followed by ImpluseDE2 and tradeSeq. Wilcoxon test does not fare well, presumably due to bias towards highly expressed genes. (**D**) The comparison of Linear TDEseq, Mixed TDEseq and ImpuseDE2 in the pattern detection accuracy under the baseline parameter settings, at an FDR of 5%. The temporal expression genes detected by TDEseq demonstrated a high accuracy than that detected by ImpluseDE2. The tradeSeq and Wilcoxon test were excluded from this comparison due to there being no shape-specific designs. (**E**) The quantile-quantile (QQ) plot shows the type I error control under the large batch effect parameter settings. The well-calibrated *p*-values will be expected laid on the diagonal line. The *p*-values generated from Mixed TDEseq coupled with scMerge (purple) are reasonably well-calibrated, while Linear TDEseq(orange), Mixed TDEseq (plum), tradeSeq (green), ImpulseDE2 (blue), and Wilcoxon test (yellow) produced the *p*-values that are not well-calibrated. (**F**) The average power of 10 simulation replicates comparison of temporal expression gene detection across a range of FDR cutoffs under the large batch effect parameter settings. (**G**) The comparison of Linear TDEseq, Mixed TDEseq, Mixed TDEseq coupled with scMerge and ImpuseDE2 in the pattern detection accuracy under the large batch effect parameter settings, at an FDR of 5%. The tradeSeq and Wilcoxon tests are excluded from this comparison due to there being no shape-specific designs. FDR denotes the false discovery rate.

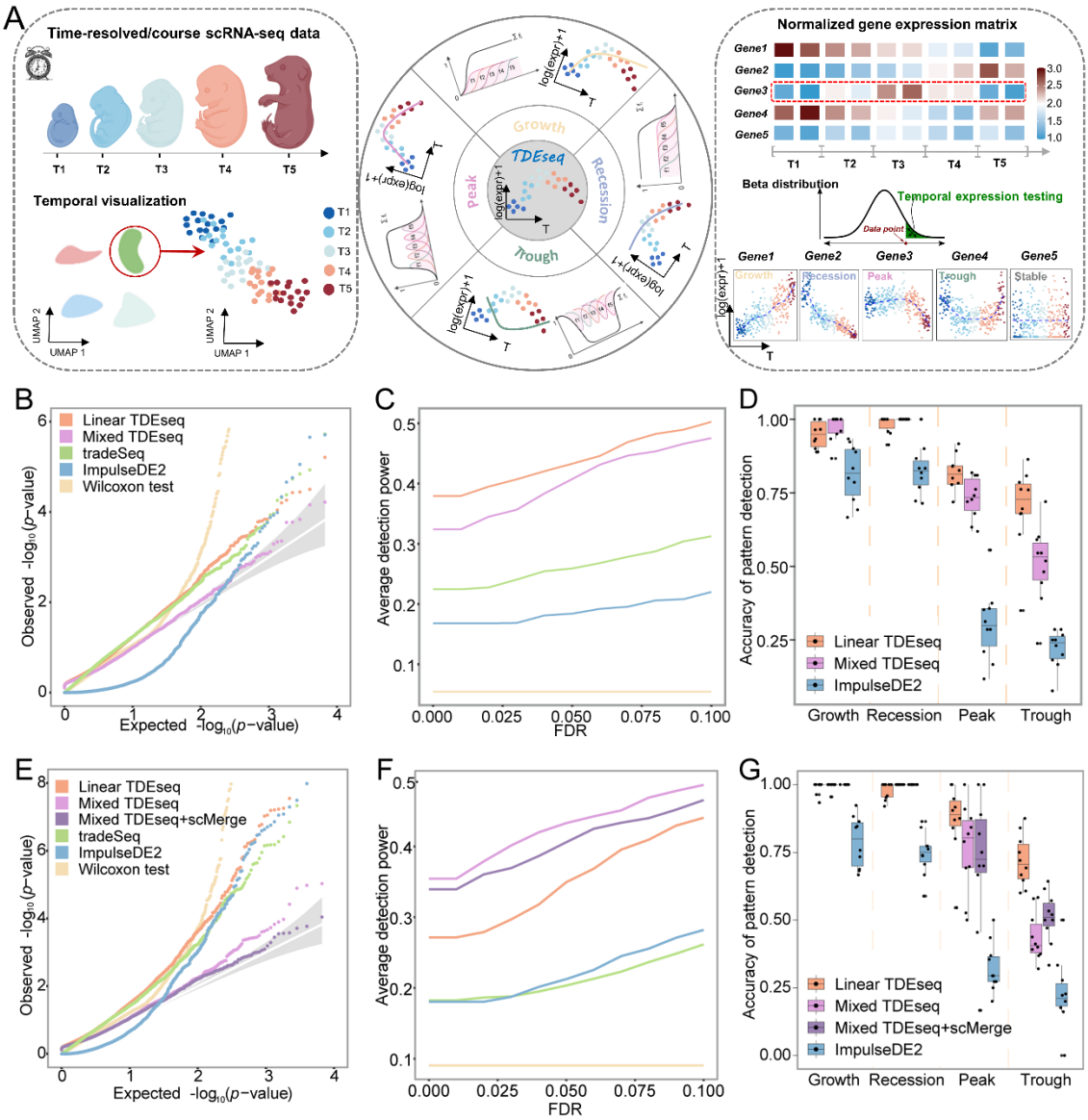
A
Time-resolved/course scRNA-seq data
T1
T2
T3
T4
T5
Temporal visualization
UMAP 2
UMAP 1
Growth
Peak
Recession
Trough
TDEseq
log(expr)+1
T
Normalized gene expression matrix
Gene1
Gene2
Gene3
Gene4
Gene5
3.0
2.5
2.0
1.5
1.0
Beta distribution
Temporal expression testing
Data point
Stable
B
Linear TDEseq
Mixed TDEseq
tradeSeq
ImpulseDE2
Wilcoxon test
Observed -log10 (p−value)
Expected -log10(p−value)
C
Average detection power
FDR
D
Accuracy of pattern detection
Growth
Recession
Peak
Trough
E
Mixed TDEseq+scMerge
F
G

Figure 2. **The time-resolved scRNA-seq data analysis for the HCT116 cell lines after 5-AZA-CdR treatment.** (**A**) The experimental design of HCT116 cell lines treated with 5-AZA-CdR. The scRNA-seq data were assayed by Well-TEMP-seq protocols, consisting of four-time points, i.e., D0, D1, D2, or D3 after treatment. (**B**) The quantile-quantile (QQ) plot shows the type I error control under the permutation strategy. The well-calibrated *p*-values will be expected laid on the diagonal line. The *p*-values produced by Linear TDEseq (red) and tradeSeq (green) are reasonably well-calibrated, while that from ImpulseDE2 (blue) are overly conservative. (**C**) The power comparison of temporal expression gene detection across a range of FDR cutoffs. Linear TDEseq displays the powerful performance of temporal expression gene detection. The Wilcoxon test was excluded from this comparison due to its poor performance in simulations. (**D**) The Venn diagram shows the overlapping of the temporally expressed genes (FDR ≤ 0.05) identified by Linear TDEseq, tradeSeq or ImpulseDE2. Those method-specific unique genes were enriched the number of GO terms (N_{GO}, BH-adjusted *p*-value < 0.05). The temporal expression genes detected by Linear TDEseq were enriched more GO terms. (**E**) The heatmap demonstrates the pattern-specific temporal expression genes that were identified by Linear TDEseq. Gene expression levels were log-transformed and were standardized using z-scores for visualization. The top-ranked temporal expression genes identified by Linear TDEseq show distinct four patterns. (**F**) The UMAP shows two temporal expression genes, i.e., *DKK1* and *IFITM3,* which were identified by Linear TDEseq but not by tradeSeq. (**G**) The Bubble plot demonstrates the significant GO terms enriched by pattern-specific temporal expression genes, which were identified by Linear TDEseq. We performed GSEA using the *clusterProfiler* R package. The peak-specific temporal expression genes enriched more significant GO terms.

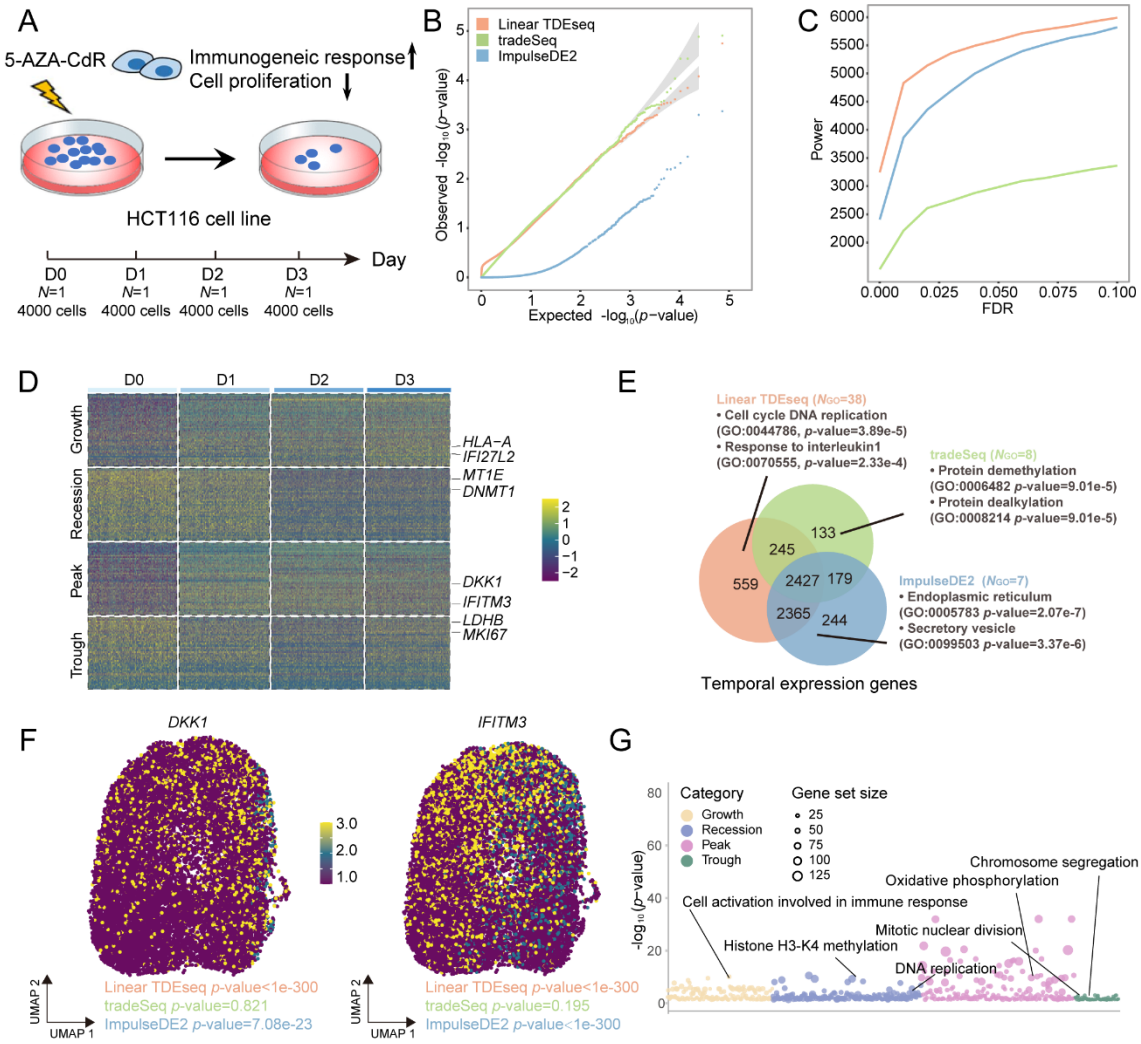
A
5-AZA-CdR
Immunogeneic response
Cell proliferation
HCT116 cell line
Day
D0 N=1 4000 cells
D1 N=1 4000 cells
D2 N=1 4000 cells
D3 N=1 4000 cells
B
Linear TDEseq
tradeSeq
ImpulseDE2
Observed -log10(p-value)
Expected -log10(p-value)
C
Power
FDR
D
D0
D1
D2
D3
Growth
Recession
Peak
Trough
HLA-A
IFI27L2
MT1E
DNMT1
DKK1
IFITM3
LDHB
MKI67
E
Linear TDEseq (NGO=38)
• Cell cycle DNA replication
(GO:0044786, p-value=3.89e-5)
• Response to interleukin1
(GO:0070555, p-value=2.33e-4)
tradeSeq (NGO=8)
• Protein demethylation
(GO:0006482 p-value=9.01e-5)
• Protein dealkylation
(GO:0008214 p-value=9.01e-5)
ImpulseDE2 (NGO=7)
• Endoplasmic reticulum
(GO:0005783 p-value=2.07e-7)
• Secretory vesicle
(GO:0099503 p-value=3.37e-6)
559
245
133
2427
179
2365
244
Temporal expression genes
F
DKK1
IFITM3
UMAP 2
UMAP 1
Linear TDEseq p-value<1e-300
tradeSeq p-value=0.821
ImpulseDE2 p-value=7.08e-23
Linear TDEseq p-value<1e-300
tradeSeq p-value=0.195
ImpulseDE2 p-value<1e-300
G
Category
Growth
Recession
Peak
Trough
Gene set size
-log10(p-value)
Chromosome segregation
Oxidative phosphorylation
Cell activation involved in immune response
Mitotic nuclear division
Histone H3-K4 methylation
DNA replication

Figure 3. **The time-course scRNA-seq data analysis for mouse fetal liver development**. (**A**) The experimental design of hepatobiliary sample collection. The scRNA-seq data were assayed on the FACS isolated cell populations, consisting of seven liver developmental stages, i.e., E10.5, E11.5, E12.5, E13.5, E14.5, E15.5, and E17.5. (**B**) The quantile-quantile (QQ) plot shows the type I error control under the permutation strategy. The well-calibrated *p*-values will be expected laid on the diagonal line. The *p*-values produced by Linear TDEseq (red), Mixed TDEseq(plum), and tradeSeq (green) are reasonably well-calibrated, while that from ImpulseDE2 (blue) are overly conservative. (**C**) The power comparison of temporal expression gene detection across a range of FDR cutoffs. Both versions of TDEseq display the powerful performance of temporal expression gene detection. The Wilcoxon test was excluded from this comparison due to its poor performance in simulations. (**D**) The heatmap demonstrates the pattern-specific temporal expression genes that were identified by Linear TDEseq. Gene expression levels were log-transformed and were standardized using z-scores for visualization. The top-ranked temporal expression genes identified by Linear TDEseq show distinct four patterns. (**E**) The Venn diagram shows the overlapping of the temporally expressed genes (FDR ≤ 0.05) identified by Linear TDEseq, tradeSeq or ImpulseDE2. Those method-specific unique genes were enriched the number of GO terms (N_{GO}, BH-adjusted *p*-value < 0.05). The temporal expression genes detected by Linear TDEseq were enriched more GO terms. (**F**) The UMAP shows two temporal expression genes, i.e., *Atf4* and *Itgb1,* which were uniquely identified by Linear TDEseq. (**G**) The Bubble plot demonstrates the significant GO terms enriched by pattern-specific temporal expression genes, which were identified by Linear TDEseq. We performed GSEA using the *clusterProfiler* R package. The recession-specific temporal expression genes enriched more significant GO terms, whereas trough-specific temporal expression genes were not enriched in any GO terms.

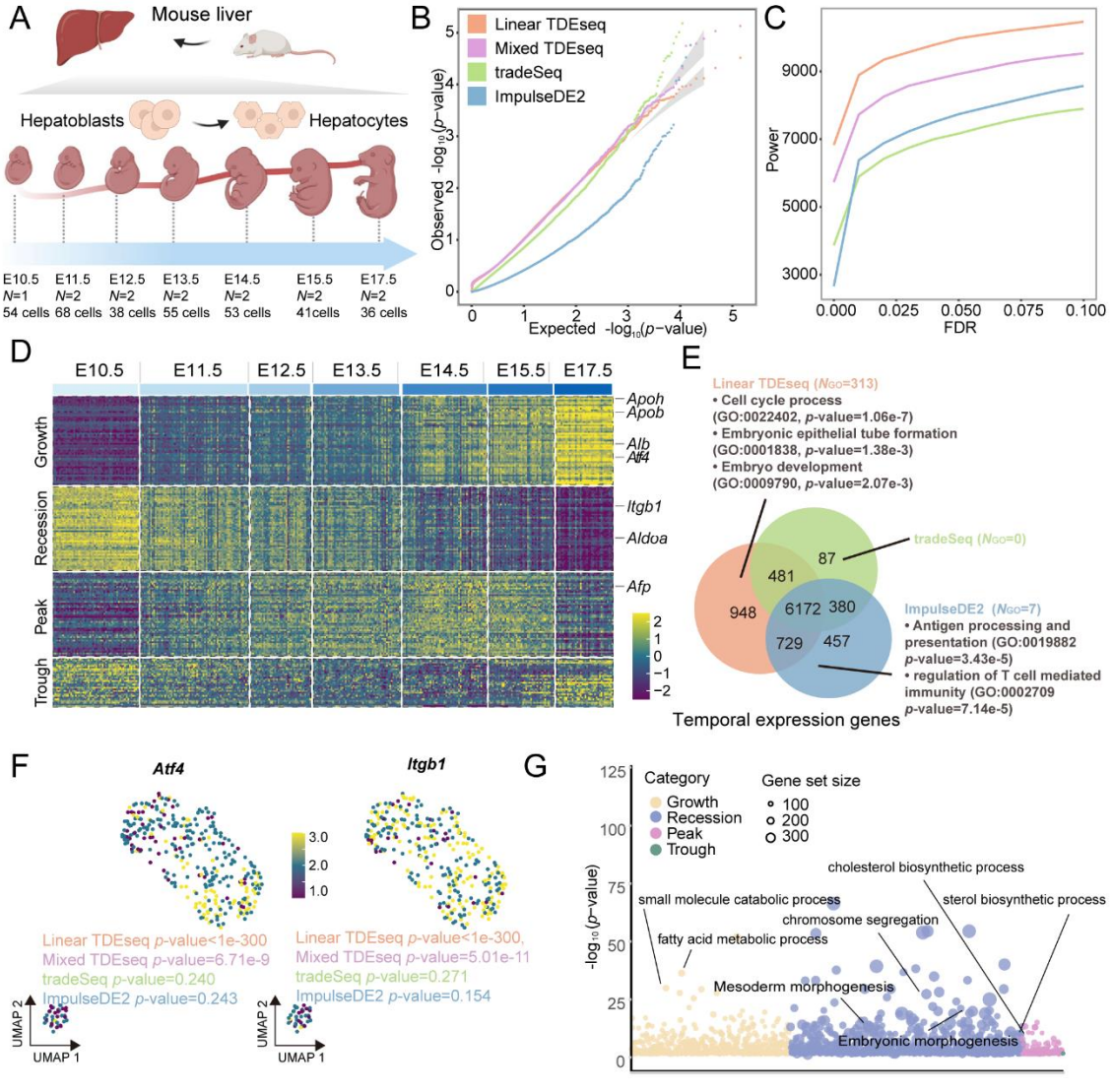
A
Mouse liver
Hepatoblasts
Hepatocytes
E10.5 N=1 54 cells
E11.5 N=2 68 cells
E12.5 N=2 38 cells
E13.5 N=2 55 cells
E14.5 N=2 53 cells
E15.5 N=2 41cells
E17.5 N=2 36 cells
B
Linear TDEseq
Mixed TDEseq
tradeSeq
ImpulseDE2
Observed -log10(p-value)
Expected -log10(p-value)
C
Power
FDR
D
E10.5
E11.5
E12.5
E13.5
E14.5
E15.5
E17.5
Growth
Recession
Peak
Trough
Apoh
Apob
Alb
Atf4
Itgb1
Aldoa
Afp
E
Linear TDEseq (NGO=313)
• Cell cycle process (GO:0022402, p-value=1.06e-7)
• Embryonic epithelial tube formation (GO:0001838, p-value=1.38e-3)
• Embryo development (GO:0009790, p-value=2.07e-3)
tradeSeq (NGO=0)
ImpulseDE2 (NGO=7)
• Antigen processing and presentation (GO:0019882 p-value=3.43e-5)
• regulation of T cell mediated immunity (GO:0002709 p-value=7.14e-5)
948
481
87
6172
380
729
457
Temporal expression genes
F
Atf4
Itgb1
Linear TDEseq p-value<1e-300
Mixed TDEseq p-value=6.71e-9
tradeSeq p-value=0.240
ImpulseDE2 p-value=0.243
Linear TDEseq p-value<1e-300,
Mixed TDEseq p-value=5.01e-11
tradeSeq p-value=0.271
ImpulseDE2 p-value=0.154
UMAP 2
UMAP 1
G
Category
Growth
Recession
Peak
Trough
Gene set size
100
200
300
-log10(p-value)
cholesterol biosynthetic process
small molecule catabolic process
sterol biosynthetic process
chromosome segregation
fatty acid metabolic process
Mesoderm morphogenesis
Embryonic morphogenesis

Figure 4. **The time-course scRNA-seq data analysis for human metastatic LUAD**. (**A**) The experimental design of human lung sample collection. The scRNA-seq data were assayed by 10X Genomics Chromium protocols, consisting of 4 LUAD evaluation stages, i.e., Normal, Stage I (early LUAD), Stage III (advanced LUAD), and Stage IV (lymph node metastasis). (**B**) The quantile-quantile (QQ) plot shows the type I error control under the permutation strategy. The well-calibrated *p*-values will be expected laid on the diagonal line. The *p*-values produced by Linear TDEseq (red), and Mixed TDEseq(plum) are reasonably well-calibrated, while that from tradeSeq (green) and ImpulseDE2 (blue) are inflated as the simulation results. (**C**) The power comparison of temporal expression gene detection across a range of FDR cutoffs. Both versions of TDEseq display the powerful performance of temporal expression gene detection. The Wilcoxon test was excluded from this comparison due to its poor performance in simulations. (**D**) The Venn diagram shows the overlapping of the temporally expressed genes (FDR ≤ 0.05) identified by Mixed TDEseq, tradeSeq or ImpulseDE2. Those method-specific unique genes were enriched the number of GO terms (N_{GO}, BH-adjusted *p*-value < 0.05). The temporal expression genes detected by Mixed TDEseq were enriched more GO terms. (**E**) The proportion of enrichment for the detected temporal expression genes. The given gene set (102 genes) was collected from ONGene [65] database. Linear TDEseq and Mixed TDEseq enriched more temporal genes than tradeSeq and ImpluseDE2. (**F**) The proportion of enrichment for the detected temporal expression genes. The given gene set (2,345 genes) was collected from the TCGA database [66]. Mixed TDEseq enriched more temporal genes than Linear TDEseq, tradeSeq, and ImpluseDE2. (**G**) The heatmap demonstrates the pattern-specific temporal expression genes that were identified by Mixed TDEseq. Gene expression levels were log-transformed and were standardized using z-scores for visualization. The top-ranked temporal expression genes identified by Mixed TDEseq show distinct four patterns. (**H**) The Bubble plot demonstrates the significant GO terms enriched by pattern-specific temporal expression genes, which were identified by Mixed TDEseq. We performed GSEA using the *clusterProfiler* R package. The peak-specific temporal expression genes enriched more significant GO terms.

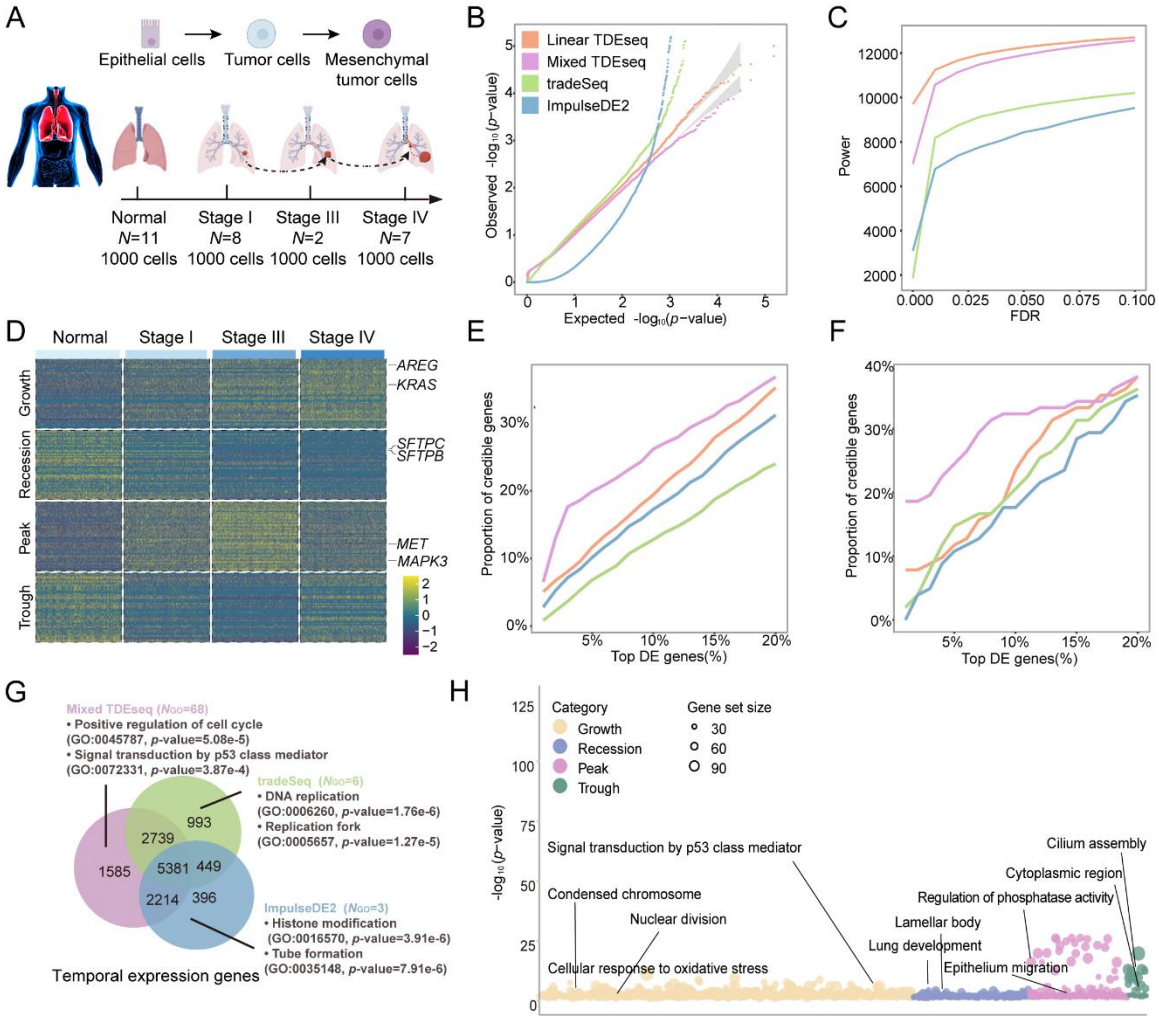
A
Epithelial cells
Tumor cells
Mesenchymal tumor cells
Normal N=11 1000 cells
Stage I N=8 1000 cells
Stage III N=2 1000 cells
Stage IV N=7 1000 cells
B
Linear TDEseq
Mixed TDEseq
tradeSeq
ImpulseDE2
Observed -log10(p-value)
Expected -log10(p-value)
C
Power
FDR
D
Normal
Stage I
Stage III
Stage IV
Growth
Recession
Peak
Trough
AREG
KRAS
SFTPC
SFTPB
MET
MAPK3
E
Proportion of credible genes
Top DE genes(%)
F
Proportion of credible genes
Top DE genes(%)
G
Mixed TDEseq (NGO=68)
• Positive regulation of cell cycle (GO:0045787, p-value=5.08e-5)
• Signal transduction by p53 class mediator (GO:0072331, p-value=3.87e-4)
tradeSeq (NGO=6)
• DNA replication (GO:0006260, p-value=1.76e-6)
• Replication fork (GO:0005657, p-value=1.27e-5)
ImpulseDE2 (NGO=3)
• Histone modification (GO:0016570, p-value=3.91e-6)
• Tube formation (GO:0035148, p-value=7.91e-6)
1585
2739
993
5381
449
2214
396
Temporal expression genes
H
Category
Growth
Recession
Peak
Trough
Gene set size
30
60
90
-log10(p-value)
Signal transduction by p53 class mediator
Condensed chromosome
Nuclear division
Cellular response to oxidative stress
Lamellar body
Lung development
Epithelium migration
Regulation of phosphatase activity
Cytoplasmic region
Cilium assembly

Figure 5. **The time-course scRNA-seq data analysis for the NK cell response to SARS-COV-2 infection**. (**A**) The experimental design of SARS-COV-2 infection samples from PBMC. The scRNA-seq data were assayed by 10X Genomics Chromium protocols, consisting of 5 stages, i.e., stage I (4-8 days), stage II (10-13 days), stage III (19-24 days), stage IV (28-34 days) and stage V (110-123 days). (**B**) The UMAP demonstrates cell alignment from different stages. These scRNA-seq data sets display strong batch effects across different evaluation stages (iLISI = 0.10, left panel). The cells are well-aligned after performing integrative analysis using scMerge (iLISI = 0.36, right panel). (**C**) The quantile-quantile (QQ) plot shows the type I error control under the permutation strategy. The well-calibrated *p*-values will be expected laid on the diagonal line. The *p*-values produced by Mixed TDEseq (plum), Mixed TDEseq coupled with scMerge (purple), and tradeSeq (green) are reasonably well-calibrated, while that from ImpulseDE2 (blue) is overly conservative. (**D**) The power comparison of temporal expression gene detection across a range of FDR cutoffs. TDEseq coupled with scMerge identified more temporal expression genes than other comparative methods. (**E**) The proportion of enrichment for the detected temporal expression genes. The given gene set (100 genes) was collected from the GO term (GO:0051607). Mixed TDEseq coupled with scMerge enriched more temporal genes than Mixed TDEseq, tradeSeq and ImpluseDE2. (**F**) The Venn diagram shows the overlapping of the temporally expressed genes (FDR ≤ 0.05) identified by Mixed TDEseq coupled with scMerge, tradeSeq and ImpulseDE2. Those method-specific unique genes were enriched the number of GO terms (N_{GO}, BH-adjusted *p*-value < 0.05). The temporal expression genes detected by Mixed TDEseq coupled with scMerge were enriched more GO terms. (**G**) The UMAP shows a recession-specific temporal expression gene, i.e., *IFI6,* which was identified by Mixed TDEseq coupled with scMerge and Mixed TDEseq, but missed by other methods. Another recession-specific gene*, IFI35,* was identified by Mixed TDEseq coupled with scMerge but missed by tradeSeq and Mixed TDEseq*.* (**H**) The overlapping of GO:0051607 term-related genes and the top-rank genes of each method. (**I**) The heatmap demonstrates the pattern-specific temporal expression genes that were identified by Mixed TDEseq coupled with scMerge. Gene expression levels were log-transformed and were standardized using z-scores for visualization. The top-ranked temporal expression genes identified by Linear TDEseq show distinct four patterns. (**J**) The Bubble plot demonstrates the significant GO terms enriched by pattern-specific temporal expression genes, which were identified by Mixed TDEseq coupled with scMerge. We performed GSEA using the *clusterProfiler* R package. The recession-specific

and peak-specific temporal expression genes enriched more significant GO terms.

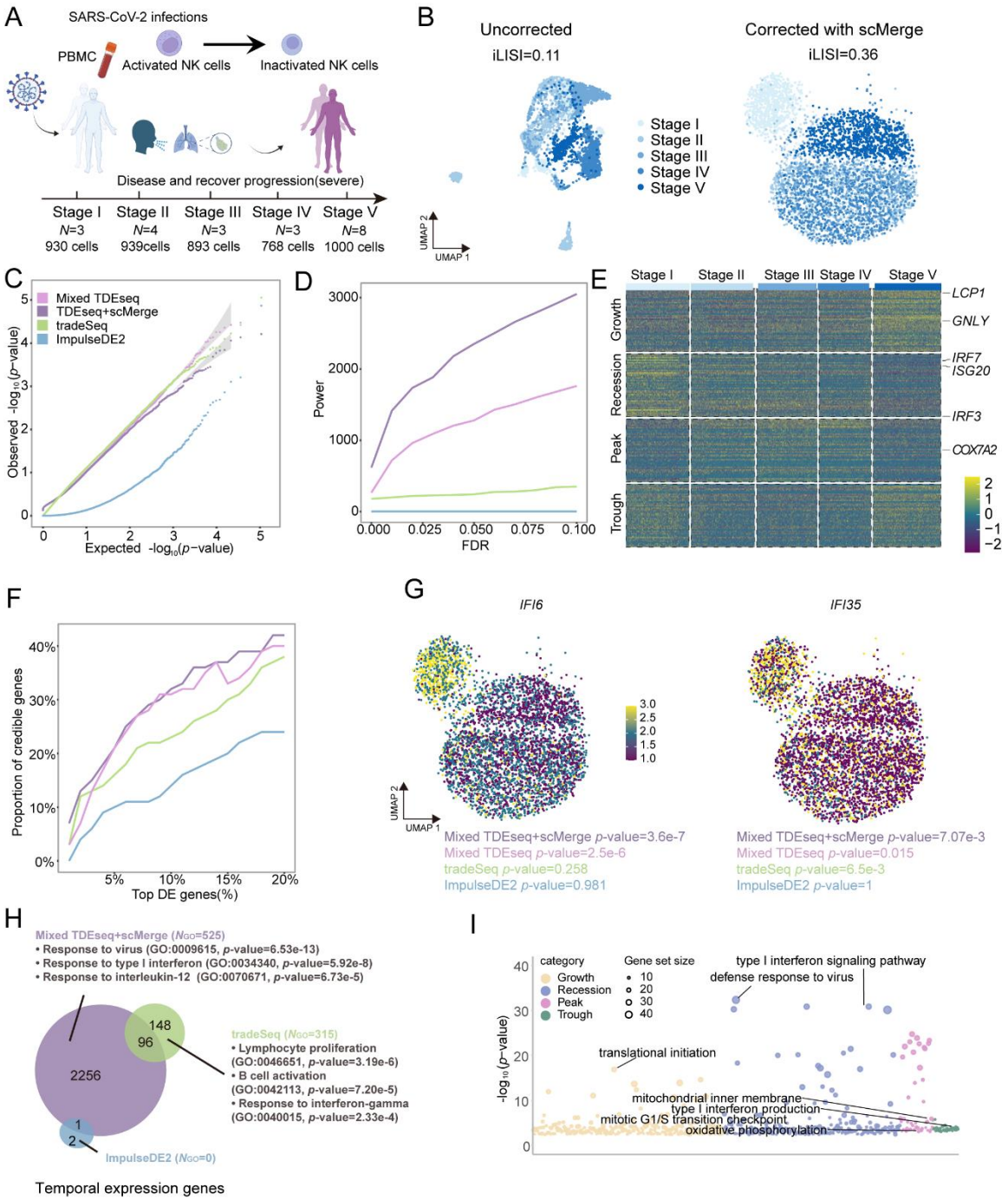
A
SARS-CoV-2 infections
PBMC
Activated NK cells
Inactivated NK cells
Disease and recover progression(severe)
Stage I N=3 930 cells
Stage II N=4 939cells
Stage III N=3 893 cells
Stage IV N=3 768 cells
Stage V N=8 1000 cells
B
Uncorrected
iLISI=0.11
Corrected with scMerge
iLISI=0.36
Stage I
Stage II
Stage III
Stage IV
Stage V
UMAP 2
UMAP 1
C
Mixed TDEseq
TDEseq+scMerge
tradeSeq
ImpulseDE2
Observed -log10(p-value)
Expected -log10(p-value)
D
Power
FDR
E
Stage I
Stage II
Stage III
Stage IV
Stage V
Growth
Recession
Peak
Trough
LCP1
GNLY
IRF7
ISG20
IRF3
COX7A2
F
Proportion of credible genes
Top DE genes(%)
G
IFI6
IFI35
Mixed TDEseq+scMerge p-value=3.6e-7
Mixed TDEseq p-value=2.5e-6
tradeSeq p-value=0.258
ImpulseDE2 p-value=0.981
Mixed TDEseq+scMerge p-value=7.07e-3
Mixed TDEseq p-value=0.015
tradeSeq p-value=6.5e-3
ImpulseDE2 p-value=1
H
Mixed TDEseq+scMerge (NGO=525)
• Response to virus (GO:0009615, p-value=6.53e-13)
• Response to type I interferon (GO:0034340, p-value=5.92e-8)
• Response to interleukin-12 (GO:0070671, p-value=6.73e-5)
2256
148
96
1
2
tradeSeq (NGO=315)
• Lymphocyte proliferation (GO:0046651, p-value=3.19e-6)
• B cell activation (GO:0042113, p-value=7.20e-5)
• Response to interferon-gamma (GO:0040015, p-value=2.33e-4)
ImpulseDE2 (NGO=0)
Temporal expression genes
I
category
Growth
Recession
Peak
Trough
Gene set size
10
20
30
40
type I interferon signaling pathway
defense response to virus
translational initiation
mitochondrial inner membrane
type I interferon production
mitotic G1/S transition checkpoint
oxidative phosphorylation
-log10(p-value)